Clim Dyn (2017) 49:2385–2406
DOI 10.1007/s00382-016-3463-2

Causes of intraseasonal diabatic heating variability over and near the Tibetan Plateau in boreal summer

Shuangyan Yang[1,2] · **Tim Li**[1,2]

Received: 16 May 2016 / Accepted: 18 November 2016 / Published online: 24 November 2016

Abstract The structure and evolution features of the first two leading modes of the intraseasonal diabatic heating variability over the Tibetan Plateau (TP) during northern summer are investigated using reanalysis and observational data. Both of the leading modes present a dominant 10–30-day intraseasonal oscillation (ISO). The first mode is characterized by a perturbation center over the southern TP (STP), which remains quasi-stationary and is closely related to the low-latitude ISO. The associated low-latitude ISO is originated from the tropical western Pacific (WP) and propagates westward/northwestward toward northwestern India along the mean monsoon trough. The westward propagation near the South China Sea is mainly attributed to anomalous meridional vorticity advection and the advection of the planetary vorticity by ISO flow. The stationary feature of the perturbation over the STP is ascribed to the topographical features around the STP. The intraseasonal heating variability over the STP is attributed to the alternation of anticyclonic and cyclonic flow associated with the westward-propagating ISO perturbation originated from the tropical WP. The second leading mode is characterized by an east–west asymmetric structure over the TP. The intraseasonal diabatic heating anomaly propagates clockwise from the northwestern to eastern TP, while a heating anomaly with an opposite sign propagates from the southeastern to western TP. The mid-latitude Rossby wave trains play an essential role in forming the dipole structure. The wave trains propagate southeastward before reaching the TP and then eastward as they cross the TP. The source of anomalous water vapor over the TP is originated from lower latitudes. The upper- and lower-level wave trains are well coupled over the TP, exhibiting a baroclinic structure.

Keywords The Tibetan Plateau · The intraseasonal oscillation · Diabatic heating anomaly

1 Introduction

The intraseasonal oscillation (ISO) appears not only over the tropics (Madden and Julian 1971, 1972; Lau and Chan 1986; Annamalai and Slingo 2001; Li and Wang 2005; Wang et al. 2006; Wen et al. 2010), but also over mid- and high-latitudes (Anderson and Rosen 1983; Krishnamurti and Gadgil 1985; Kikuchi and Wang 2009; Wang et al. 2013; Yang et al. 2013b). Large-scale circulations associated with the ISO may affect tropical cyclone activities (Maloney and Hartmann 2000; Xu et al. 2014; Bi et al. 2015), rainfall or temperature anomalies over continent (Hoyos and Webster 2007; Mao et al. 2010; Yang et al. 2010, 2013a; Yang and Li 2016a), onset of the monsoon (Zhang et al. 2002; Lorenz and Hartmann 2006; Jia and Yang 2013), and ENSO activities (Rong et al. 2011; Chen et al. 2016).

The Tibetan Plateau (TP) has been known as the third pole of the world. Its mean elevation is 4000–5000 m above sea level, reaching almost to the mid-troposphere. Due to

✉ Tim Li
timli@hawaii.edu

[1] Key Laboratory of Meteorological Disaster, Ministry of Education (KLME)/Joint International Research Laboratory of Climate and Environmental Change (ILCEC)/ Collaborative Innovation Center on Forecast and Evaluation of Meteorological Disasters (CIC-FEMD), Nanjing University of Information Science and Technology, Nanjing, China

[2] International Pacific Research Center and Department of Atmospheric Sciences, University of Hawaii at Manoa, Honolulu, HI 96822, USA

its thermal effect in the mid-troposphere, it profoundly affects the general circulation in the Northern Hemisphere (Ye 1981; Ye and Wu 1998; Duan and Wu 2005; Wu et al. 2007; Duan et al. 2008, 2013; Zhou et al. 2009), including the Asian monsoon (e.g., Flohn 1957; Yanai et al. 1992; Li and Yanai 1996; Sato and Kimura 2007; Wu et al. 2012) and global hydrological cycle (e.g., Tao and Ding 1981; Zhao and Chen 2001; Wang et al. 2008, 2014; Yang et al. 2014).

Many previous studies demonstrated the intraseasonal variability around the TP including South Asia (e.g., Annamalai and Slingo 2001; Chatterjee and Goswami 2004; Fujinami et al. 2011, 2014). Bangladesh is located to the south of the TP, and lies in few latitudes away from the TP. Fujinami et al. (2011) reported that a sub-monthly mode is predominant in the summer precipitation over Bangladesh. Detailed characteristics of the sub-monthly variation in summer rainfall and circulation fields over the Meghalaya-Bangladesh-western Myanmar area have been revealed in Fujinami et al. (2014). As the TP is closely related to the climate of the Asian area (Flohn 1957; Duan et al. 2008), there should be a relevant intraseasonal variation over the TP. The heat source and associated dynamic and thermodynamic variables (e.g., precipitation, relative vorticity, air temperature, wind and geopotential height) over the TP show a marked intraseasonal oscillation (e.g., Krishnamurti and Subrahmanyam 1982; Nitta 1983; Fujinami and Yasunari 2001; Wang and Duan 2015). Nitta (1983) revealed that the total heating over the eastern TP fluctuates with ~12-day and ~30-day periods. Fujinami and Yasunari (2001) reported that summer convection over the TP presents a periodicity of ~15 and ~30 days. Wang and Duan (2015) identified a 10–20-day oscillation of the heat source as well as the circulation fields over the TP. On the intraseasonal time scale, the TP plays an important role in the Asian summer monsoom (Fujinami and Yasunari 2009; Wang and Duan 2015).

The heat source and moisture sink show different features between the eastern and western TP (Luo and Yanai 1984; Ueda et al. 2003). The land cover over the TP shows an obvious difference between eastern and western parts (Cui and Graf 2009), which can affect the behavior of clouds and rainfall through modulating the local heating in summer (Chen et al. 2015). The southern TP composes the Asian summer monsoon as one main component (Murakami and Matsumoto 1994). The above mentioned studies suggest that the intraseasonal heating variability over the TP maybe exhibit different spatial patterns, which has not been fully understood yet. Fujinami and Yasunari (2004; hereafter FY04) showed that there is a maximum convection center over the southern TP in climatological summer, and the regional mean convection over the southern TP shows a significant sub-monthly (7–20-day) oscillation. Note that FY04 used equivalent blackbody temperature (Tbb) data as an index of cloud cover. When precipitation data was used, the maximum center appears over the southeastern TP. The associated convection oscillation exhibits a clockwise rotation around about 28°N, 90°E, along a pathway of TP—Indochina—the Bay of Bengal—India. By using various datasets, Wang and Duan (2015; hereafter WD15) revealed that there is a predominant periodicity in the band of 10–20 days (quasi-biweekly oscillation, QBWO) in various fields. Referring to a location at 27°N along 70°–100°E, WD15 reported that the propagating QBWO (from the low latitudes to the TP) shows a clockwise propagation, by a pathway of equatorial western Pacific—the Bay of Bengal—northern India—southeastern TP—the eastern Asia. The above results suggest that different ISO patterns appear over the TP. The objective of the current study is two folds. Firstly we intend to identify the principal modes of the intraseasonal variation of diabatic heating over and near the TP (including the Himalayas and Meghalaya Plateau) in boreal summer based on the empirical orthogonal function (EOF) analysis. Secondly we will further investigate the origin of the intraseasonal heating variability over and near the TP.

The rest of this paper is organized as follows. In Sect. 2, data and methodology are described. The dominant mode of the intraseasonal diabatic heating anomaly over and near the TP is analyzed in Sect. 3, including its spatial pattern, evolution characteristics, and possible mechanisms of the evolutions. In Sect. 4, the second leading mode is further identified, including its structure, evolution, and possible causes of the formation of this mode. Summaries are concluded in Sect. 5.

2 Data and methodology

The reanalysis data at a 1.5° × 1.5° horizontal resolution and 37 vertical levels for the period of 1979–2014 derived from the European Centre for Medium-Range Weather Forecasts (ECMWF) Interim reanalysis (ERA-Interim; Dee et al. 2011) are used in this study. We average the original 4-time daily data to create the daily mean datasets. The ERA-Interim datasets have already been used to study the intraseasonal variation over the TP in WD15. Daily outgoing longwave radiation (OLR) at a 2.5° × 2.5° horizontal resolution during 1979–2010 derived from the National Oceanic and Atmospheric Administration (NOAA) polar-orbiting satellites (Liebmann and Smith 1996) is used as a proxy for convection. Also used is the daily precipitation at a horizontal resolution of 0.5° × 0.5° during 1979–2007 derived from Asian Precipitation-Highly-Resolved

Observational Data Integration Towards Evaluation project (APHRODITE; Hamada et al. 2011, Yatagai et al. 2012). The APHRODITE precipitation is a state-of-the-art dataset for Asia covering the land only. This dataset is produced primarily with data obtained from a rain-gauge-observation network. Fujinami et al. (2014; hereafter FY14) have already used this dataset to investigate the sub-monthly variations around South Asia. Also used is the daily precipitation from Global Precipitation Climatology Project (GPCP; Huffman et al. 2001) at a horizontal resolution of $1° \times 1°$ during 1997–2014.

According to Yanai et al. (1973), the vertically integrated apparent heat source $\langle Q_1 \rangle$ and moisture sink $\langle Q_2 \rangle$ are calculated as residuals of the thermodynamic and moisture equations, respectively. Velocity potential and divergent wind at pressure levels are also calculated using daily mean ERA-Interim data. To confirm the ERA-Interim reanalysis data can reproduce a reasonable temporal evolution over the TP, daily precipitation data from 1979 to 2008, obtained from National Meteorological Information Center of China Meteorological Administration, at 34 observational stations over the TP are also used.

The ISO signals for each field are isolated by three steps. First, the annual cycle and its first four harmonics are removed to get a non-filtered anomaly field. Second, the obtained anomalies are subject to a 5-day running mean to remove the synoptic turbulence. Third, a filtered anomaly field is derived by a Lanczos bandpass filter (Duchon 1979). The ISO signals in each summer (June–July–August, JJA) are abstracted finally.

3 The first leading mode of diabatic heating over the TP

3.1 Climatological feature

Prior to analyzing the leading modes of diabatic heating over the TP, we first illustrate the climatological summer-mean distribution of the diabatic heating and APHRODITE precipitation. The precipitation pattern is characterized by an enhanced rainfall in the windward areas around the southern TP, especially over the southern slope of Himalayas (Fig. 1a). The precipitation pattern obtained from GPCP exhibits a similar feature (figure omitted). The features of enhanced rainfall resulting from reginal-scale terrain have also noted by previous studies (e.g., FY14). As shown in Fig. 1b, large $\langle Q_1 \rangle$ appears over and near the southern TP including Himalayas and Meghalaya Plateau. In this study, we select the TP-Himalayas-Meghalaya Plateau region to explore the leading modes of the $\langle Q_1 \rangle$.

To judge whether or not the ERA-Interim reanalysis can reproduce a reasonable spatial distribution, the $\langle Q_2 \rangle$ which is chiefly related to the condensational heating is displayed in Fig. 1c. It is found that the spatial feature of the $\langle Q_2 \rangle$ agrees well with that of the precipitation shown in Fig. 1a, especially over the southern TP—Himalayas–Meghalaya Plateau regions. To further confirm the reanalysis can reproduce a reasonable temporal evolution, the time series of a regional mean (boxed area in Fig. 2a) $\langle Q_2 \rangle$ and a station-averaged (dots in Fig. 2a) rainfall are compared (Fig. 2b). The correlation coefficient between them reaches

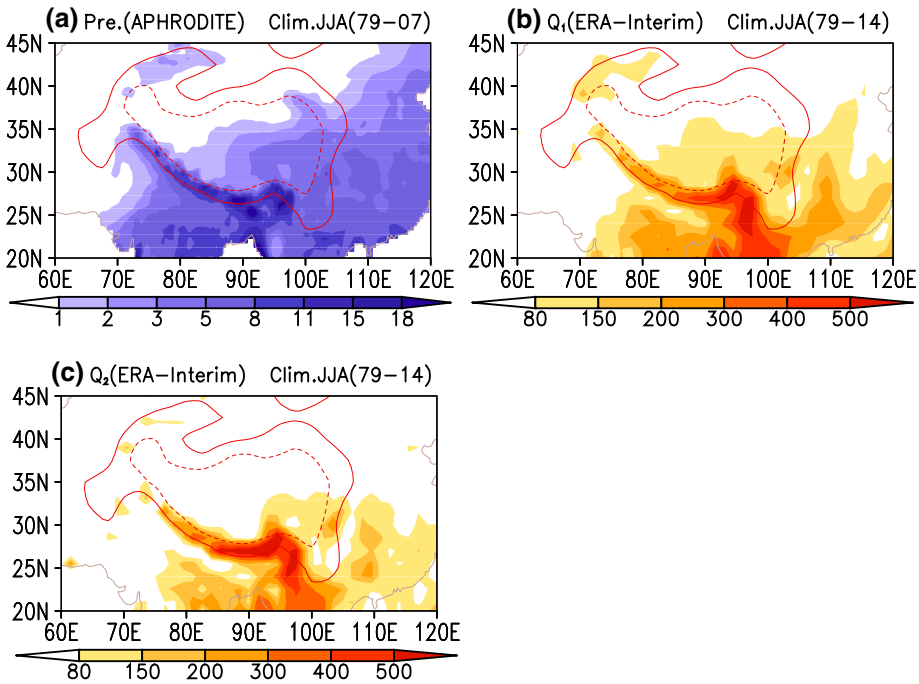

Fig. 1 Distribution of the climatological summer (JJA) mean **a** APHRODITE precipitation (1979–2007; mm day^{-1}), **b** $\langle Q_1 \rangle$ and **c** $\langle Q_2 \rangle$ calculated using the ERA-Interim reanalysis (1979–2014; W m^{-2}). *Red* solid (*dashed*) contour denotes topography exceeding 1500 m (3000 m), the same as below

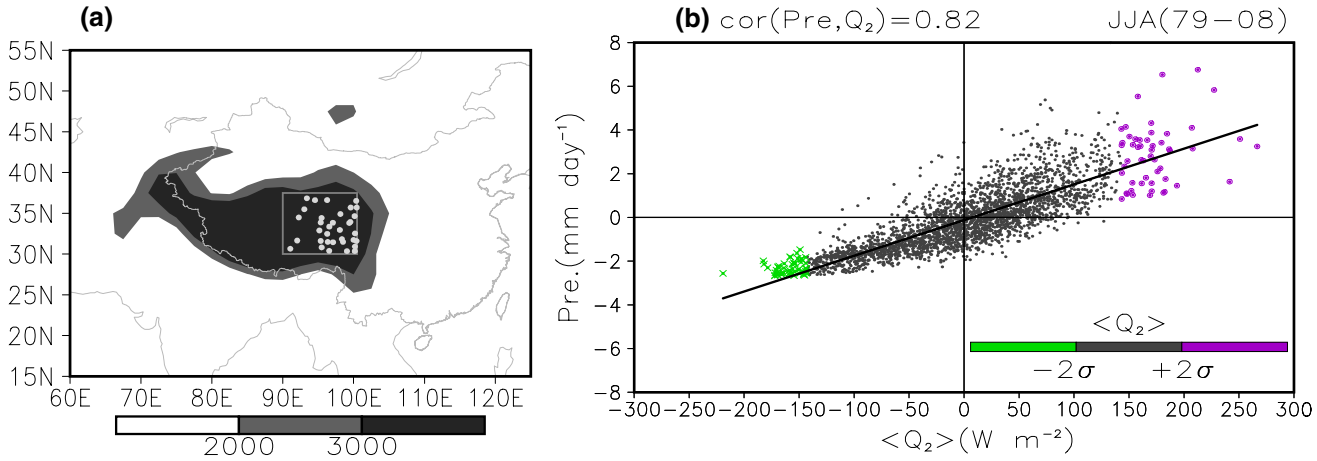

Fig. 2 **a** Geographical position of observational stations (*dots*) located in a regional area (*box*); *shading* denotes the topography. **b** Comparisons of box-averaged $\langle Q_2 \rangle$ and station-averaged rainfall (with the seasonal cycle removed); *purple dots* (*green* corosses) indicate $\langle Q_2 \rangle$ greater (less) that +2 (−2) standard deviations

~0.82, exceeding the 0.01 significance level. Moreover, the maximum rainfall corresponds to the greatest value of $\langle Q_2 \rangle$ (see purple dots), and the minimum rainfall to the lowest $\langle Q_2 \rangle$ (see green crosses). The analysis above indicates that the ERA-Interim reanalysis can reproduce both the spatial distribution and temporal evolution well compared to the observed data over and near the TP.

3.2 Spatial pattern and evolution feature

The EOF analysis is used to get a dominant pattern of the non-filtered $\langle Q_1 \rangle$ anomaly over the TP. The variance contribution of the first three modes is 12.5, 6.5 and 4.6%, respectively. As shown in Fig. 3a, the first mode (EOF1) pattern exhibits a perturbation center over the southern TP (STP). The pattern of the standard deviation (STD) of the non-filtered $\langle Q_1 \rangle$ anomaly exhibits a maximum center also over the STP (Fig. 3b). One may notice that the high variance appears over the southern slope of the Himalayas. To avoid the effect of the region south of the TP, we select a region of 28.5°–40.5°N, 70.5°–105°E, in which the Himalayas and the Meghalaya Plateau are excluded, to perform an EOF analysis again. The so-calculated EOF1 pattern is also characterized by a perturbation center over the STP (figure omitted). Thus, the result obtained from the EOF analysis in this study is not sensitive to the choice of analysis domain. Moreover, according to Fujinami et al. (2011) and FY14, there exists a dominant QBWO mode to the south of the Himalayas. By using station observational data, WD15 revealed that the QBWO is a predominant mode over the TP. Hence, it seems reasonable to consider the Tibetan Plateau-Himalayas-Meghalaya Plateau region as a whole. In subsequent Sects. 3 and 4, Himalayas-Meghalaya Plateau regions are included, once the "STP" is mentioned, unless indicated otherwise.

To obtain the dominant period, a power spectrum analysis is subject to an area-averaged (the rectangle region of 25.5°–31.5°N, 79.5°–100.5°E) $\langle Q_1 \rangle$ anomaly (Fig. 3c). It is seen that the statistically significant peak appears in the 10–30-day band. The same significant period is also detected in $\langle Q_2 \rangle$ anomaly (Fig. 3d) and 500-hPa geopotential height anomaly (Fig. 3e). Next, we will examine the perturbation features associated with the intraseasonal variability of 10–30 days.

The EOF1 pattern of the filtered $\langle Q_1 \rangle$ anomaly also exhibits a center over the STP (Fig. 3f). The fractional variance explained by the first four EOF modes is shown in Table 1. It is seen that the EOF1 and EOF2 are statistically distinguished from the third mode. What's more, the first two modes are statistically separable from each other in terms of the sampling error (see Table 1), referring to the method proposed by North et al. (1982). Similar to Wang et al. (2013) and Yang and Li (2016a), a composite analysis is used to diagnose the evolution of the ISO perturbation associated with this leading mode. Based on the first principal component (PC1) time series, a total of 69 positive and 69 negative extremes which exceed 1.5 standard deviations are selected for composite. Daily lead-lag composites of various anomaly fields are conducted by reference to these extreme days (i.e., day 0). As the negative case composite nearly exhibits a mirror image of the positive case composite, the difference between them (positive minus negative) is examined in the subsequent text.

Figure 4 shows the evolution patterns of the $\langle Q_1 \rangle$ and OLR anomalies from day −12 to +6, at an interval of 2 days. The evolution of the composite OLR anomaly (contours) as well as the GPCP rain anomaly (not shown) is highly consistent with that of the $\langle Q_1 \rangle$ anomaly. At day −12, a maximum $\langle Q_1 \rangle$ anomaly center is located over the

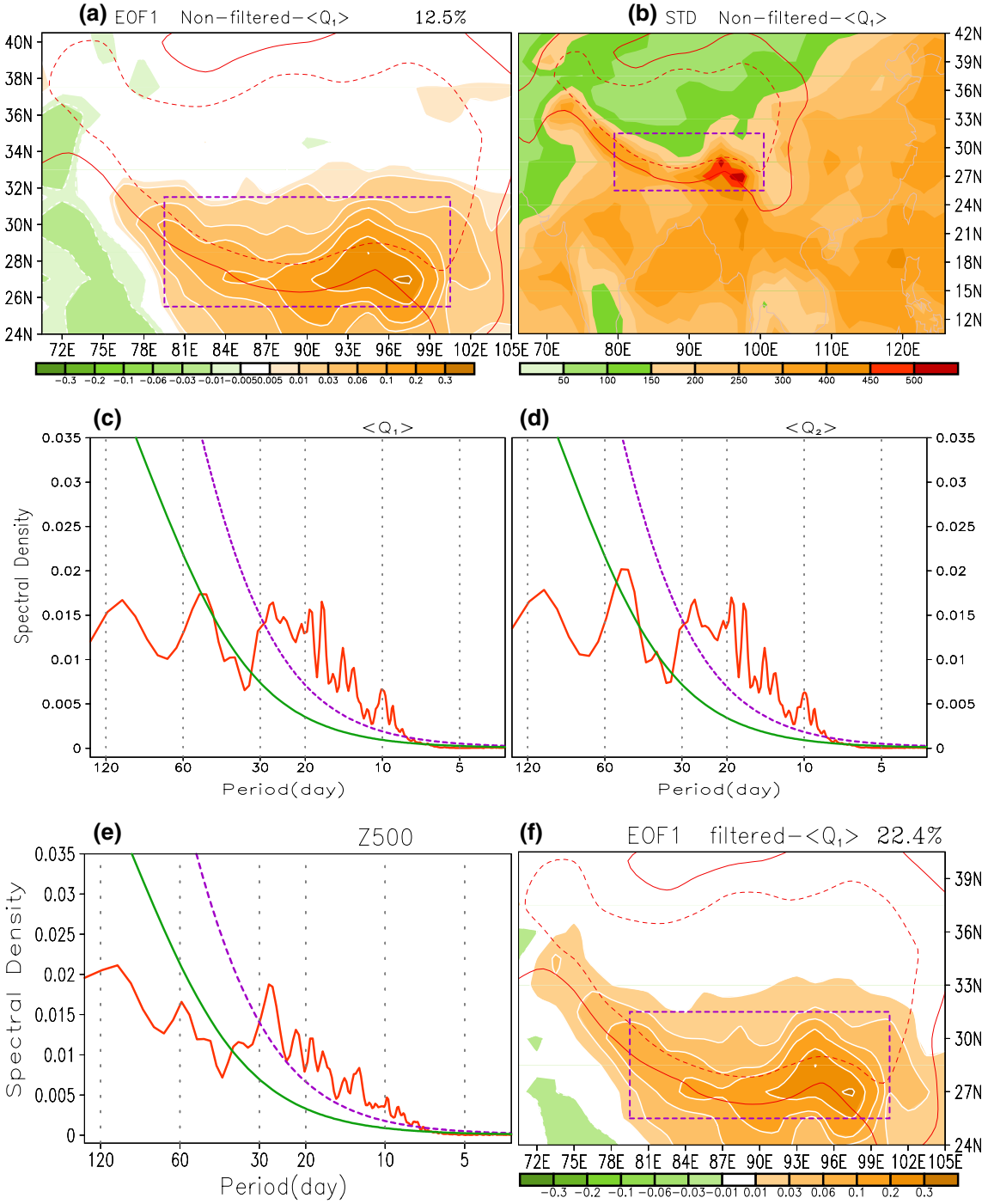

Fig. 3 **a** EOF1, and **b** standard deviation (W m^{-2}) of non-filtered $\langle Q_1 \rangle$ anomaly in JJA. Power spectral analysis of **c** $\langle Q_1 \rangle$, **d** $\langle Q_2 \rangle$, and **e** 500 hPa-geopotential height anomalies averaged over the box region. **f** EOF1 of 10–30-day filtered $\langle Q_1 \rangle$. *Solid* and *dashed lines* in (**c**)–(**e**) is spectrum density of red noise and the 0.01 significance level, respectively

South China Sea (SCS). This perturbation originates from the tropical western Pacific suggested by the evolution patterns at previous days. At day −10, the perturbation intensifies and extends to the Bay of Bengal (BOB). From day −8 to −4, the perturbation continues to propagate northwestward and stretches over the northwestern India by day −4. During these days (−8 to −4), a negative $\langle Q_1 \rangle$ anomaly is located over the STP. At day −2, the $\langle Q_1 \rangle$ anomaly over the STP changes its sign quickly. This positive $\langle Q_1 \rangle$ anomaly reinforces and reaches its maximum

Table 1 Fractional variance (%) explained by the first four EOF modes of the filtered $\langle Q_1 \rangle$ anomaly and the associated unit standard deviation of the sampling errors

EOF1	EOF2	EOF3	EOF4
22.4 ± 1.29	6.7 ± 0.39	5.2 ± 0.30	4.8 ± 0.28

The effective sample sizes are estimated referring to Bretherton et al. (1999)

over the STP at day 0. From day −2 to +2, the positive $\langle Q_1 \rangle$ anomaly (with negative OLR anomaly) over the STP remains quasi-stationary, similar to the negative $\langle Q_1 \rangle$ anomaly (with positive OLR anomaly) from day −8 to −4. During these days (−2 to +2), a negative $\langle Q_1 \rangle$ anomaly (with positive OLR anomaly), which also originates from the tropical western Pacific (see day −8), reaches the BOB and northwestern India in sequence. At day +4, the perturbation over the STP attenuates, and then alters its sign at day +6 when a positive $\langle Q_1 \rangle$ anomaly (with a negative OLR anomaly) reaches the BOB. The perturbation from the SCS propagates northwestward toward the northwestern India along the mean monsoon trough. Once the perturbation reaches the BOB and Indian sector, it could propagate northward to the TP, which has been well illustrated in WD15. WD15 suggested two mechanisms (i.e., vertical shear mechanism and a moisture advection effect) that lead to the northward propagation of the QBWO over the Indian sector. In this study (next subsection), we will propose another process that causes the intraseasonal variability over the STP. It is observed that the ISO perturbations over tropical western Pacific and the SCS can gradually move to the eastern China (e.g., from day −12 to −6), indicating the impact of the tropical ISO on the weather and climate change in China.

To confirm the evolution feature above, the patterns of the moisture condition are shown in Fig. 5. Generally, a positive $\langle Q_1 \rangle$ center is associated with a moisture convergence. It is noted that $\langle Q_1 \rangle$ and OLR perturbations over the STP undergo a strengthening from day −2 to day 0 (Fig. 4). A reason for the strengthening of the perturbations is that an anticyclonic anomaly propagates westward from the western Pacific onto the BOB, and then enhances the southwesterly flow (marked as "SW" in Fig. 5) toward the areas to the south of the TP. This leads to more moisture transport to the STP and an evident moisture convergence over the STP due to the topographical feature around the STP. Therefore, the convective activities become exuberant, inducing the intensifying of convective heating. Of most obviousness is that the $\langle Q_1 \rangle$ (shadings in Fig. 4) and moisture flux divergence (shadings in Fig. 5) anomalies do not move but remain quasi-stationary over the STP, although the perturbations from the SCS to the BOB move westward. However, the evolution of the vertically integrated water vapor flux mainly reflects the lower-troposphere circulation features. The mid- and upper-tropospheric circulation associated the ISO mode will be discussed in the next subsection to further examine the cause of the intraseasonal variability over the STP.

The propagation feature of ISO perturbations can be readily displayed by the hovmöller diagrams of the composite fields. Figure 6a, b shows the time-longitude pattern of the $\langle Q_1 \rangle$ (OLR) anomaly averaged along 10.5°–15°N (10°–15°N). These patterns clearly illustrate the westward propagation (see red arrows). Over the BOB (regions between the two blue lines), the perturbations can successively propagate northward to near 20°N (Fig. 6c, d). The stationary feature over the STP is also seen obviously. Of most importance is that the mechanisms of the variation in the anomalies over the BOB (marked by "A") and over the STP (marked by "B") are quite different from each other. The variation over the BOB directly results from the westward-propagating ISO originated from the western Pacific. As implied in the above paragraph, it is not a successive process from the BOB (related to "A") to the STP (related to "B"). One process through which the convection or heating anomalies over the STP varies will be discussed in the next subsection.

It seems that the evolution features of the first leading mode are related to those revealed in both FY14 and WD15, although the key area for the composite analysis in FY14 is 20°–26°N, 88°–93°E obtained from rainfall data and the composite analysis is referred to the location at 27°N along 70°–100°E in WD15. It is worth noting that the distributions of the perturbations in this study are somewhat similar to those in WD15, but in this study we focus on a different process, in which the perturbations over the STP is not directly caused by a successive propagation of the perturbations over the BOB or northwestern India. In addition, we reveal the STP mode is dominant over the TP, in which the perturbation over the STP remains quasi-stationary. However, in WD15 they demonstrated the propagating ISO mode (from low latitudes to the TP, i.e., type-I in WD15) is predominant over the TP, in which the perturbation over the TP can further move northward and eastward to the East Asian area. Both of the results are validated with each other by some similarities of the ISO evolution between WD15 and this study.

3.3 Mechanism of the perturbation evolutions

At low latitudes, the perturbation originated from the tropical western Pacific propagates westward/northwestward from the SCS to the BOB and northwestern India along the mean monsoon trough. The analyses in previous subsection suggest that this propagating ISO is closely related to the intraseasonal variability over the STP. In the following, we

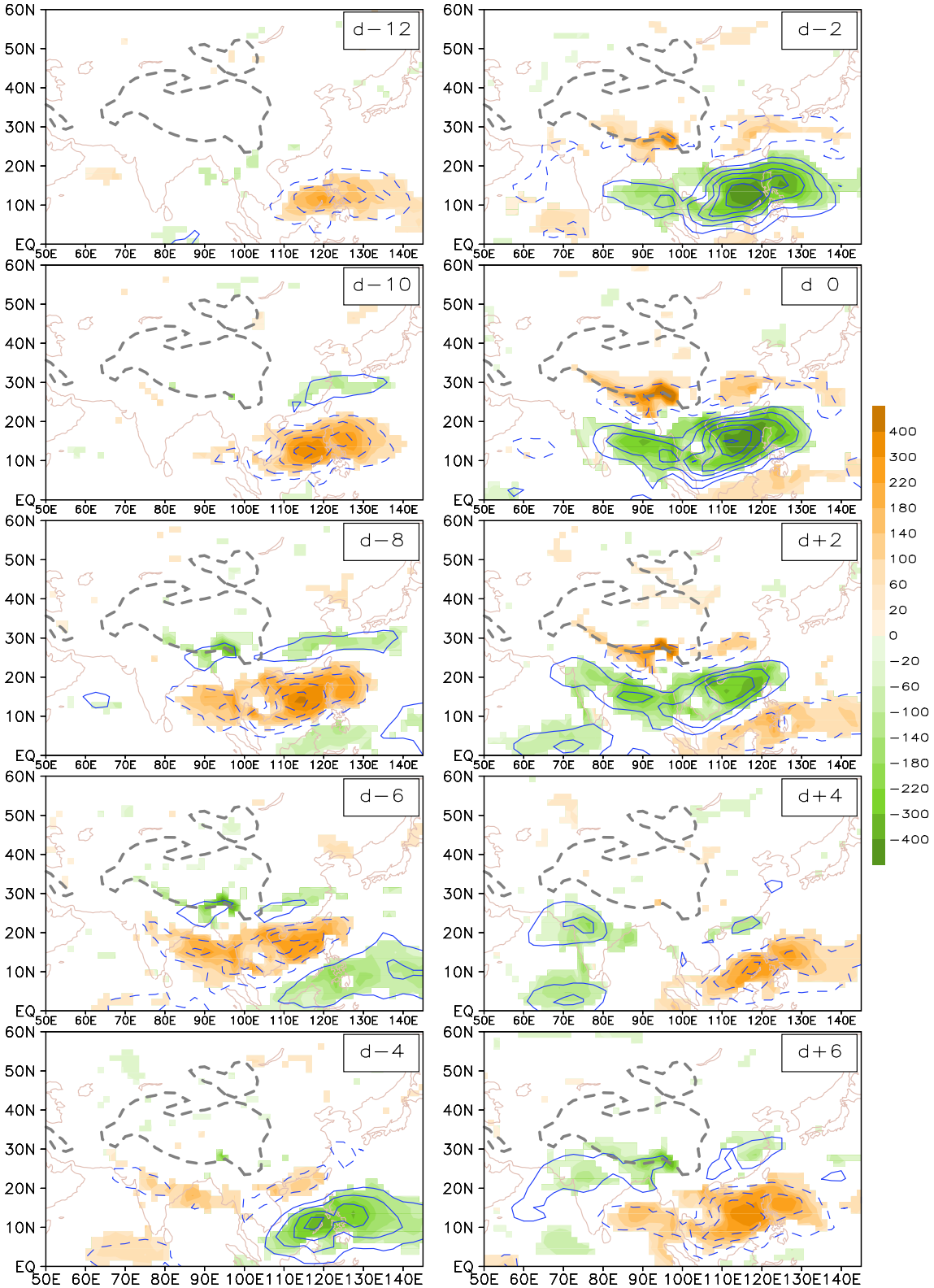

Fig. 4 Composite of 10–30-day filtered $\langle Q_1 \rangle$ (*shading*; W m^{-2}) and OLR (contour with interval of 12 W m^{-2}; zero contour is omitted) from day −12 to +6. *Shadings* and contours exceed the 0.05 significance level. *Gray* contour denotes topography exceeding 1500 m

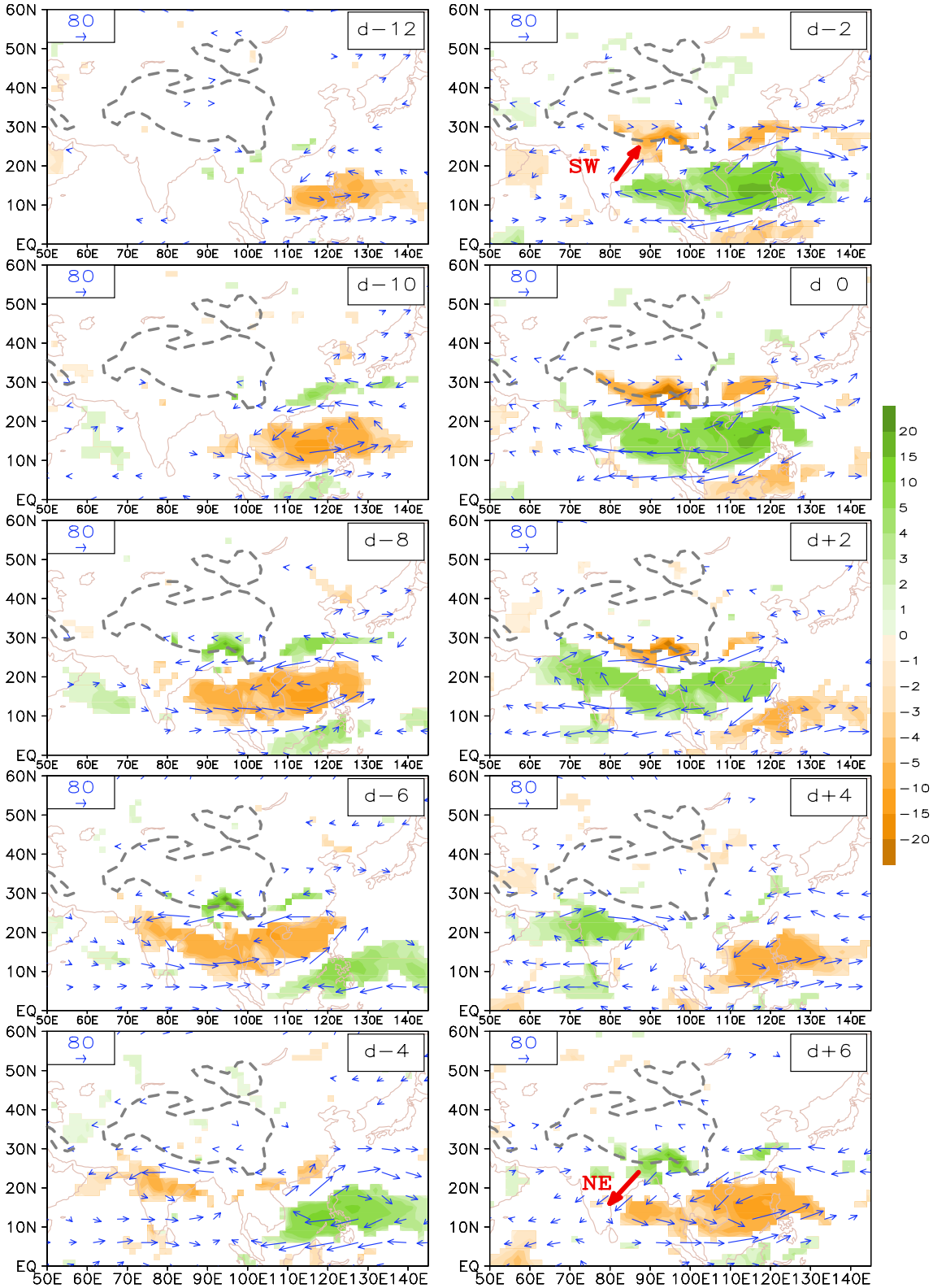

Fig. 5 As in Fig. 4, but for 10–30-day vertically integrated water vapor flux (*vector*; kg m^{-1} s^{-1}) and moisture flux divergence (*shading*; 10^{-5} kg m^{-2} s^{-1}). *Red arrow* indicates a southwesterly ("SW") or northeasterly ("NE") flow, the same as bellow. *Shadings* and *vectors* exceed the 0.05 significance level

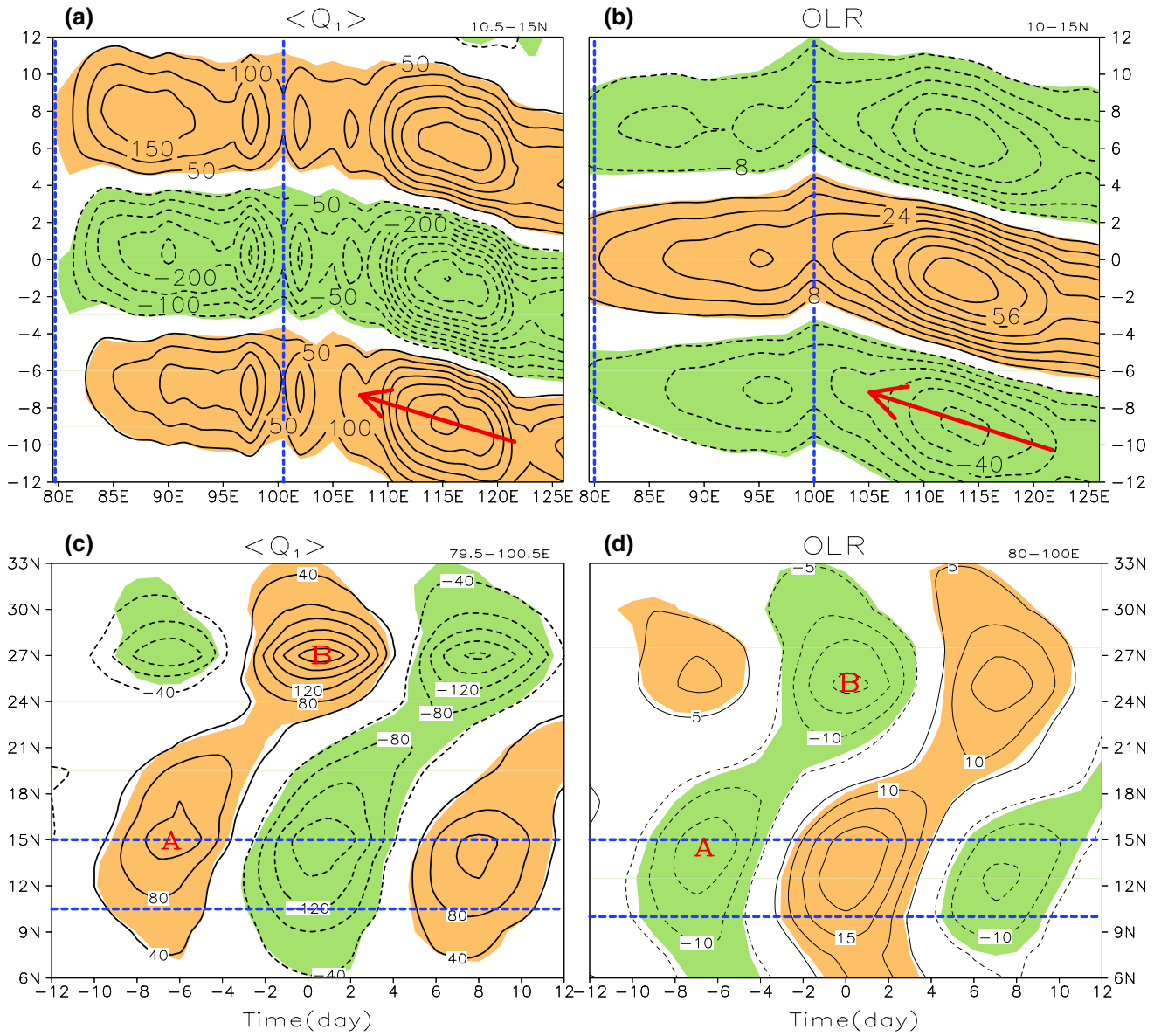

Fig. 6 Time-longitude distribution of composite 10–30-day filtered **a** $\langle Q_1 \rangle$ and **b** OLR. **c**, **d** As in (**a**), (**b**), but for latitude-time distribution. Zero contours are omitted; *shadings* surpass the 0.05 significance level. Area between *dashed lines* in (**a**), (**b**) denotes the target region of (**c**), (**d**); area between *dashed lines* in (**c**), (**d**) denotes the target region in (**a**), (**b**). "*A*" and "*B*" in (**c**), (**d**) indicated two perturbation center. Unit is W m^{-2}

intend to discuss the possible mechanism of the propagation at low latitudes and the cause of the intraseasonal variability over the STP.

3.3.1 Mechanism of propagation at low latitudes

There is a certain amount of consensus that the westward-propagating ISO originated from the western Pacific comes from the equatorial Rossby waves (e.g. Chen and Chen 1993; Annamalai and Slingo 2001; Chatterjee and Goswami 2004; Yokoi and Satomura 2005; Kikuchi and Wang 2009; FY14; WD15). Based on the axis of the maximum perturbation, the average zonal phase speed of the Rossby wave is estimated to be 6.2–7.5 m s^{-1}, which is consistent with those in previous studies (about 4–8 m s^{-1}) as summarized in Yokoi and Satomura (2005).

To further explore the possible mechanism of the westward propagation of the ISO, referring to Jiang et al. (2004) and WD15, each zonal structure is first constructed for a given field based on the longitude distance from each

convection center (where the maximum $\langle Q_1 \rangle$ or minimum OLR anomalies occur) over the SCS (where an obvious westward propagation occurs; see Fig. 6a, b), and then the anomalies with the same longitude distance are averaged because of the similarity of these meridional structures. The zonal-vertical structure of the composite ISO fields with respect to the maximum convection location is shown in Fig. 7. It is seen that the asymmetries of the anomaly fields are not obvious, except for the vorticity anomaly filed. Thus, in the following we perform a vorticity budget analysis to reveal the primary contributor to the westward propagation. The tendency of the relative vorticity equation can be written as (Holton 1992):

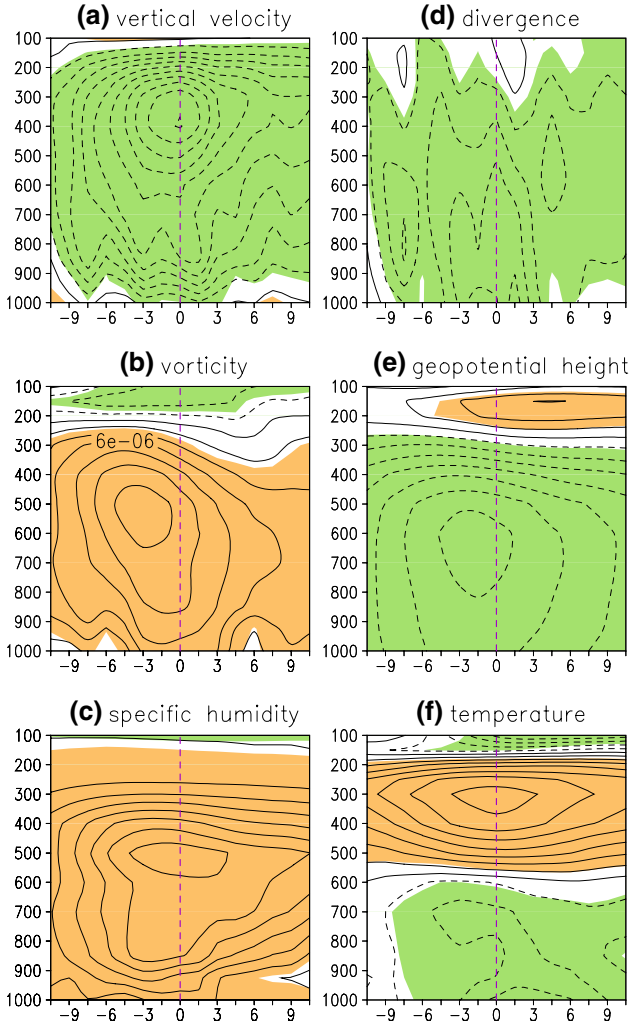

Fig. 7 Zonal-vertical distribution of 10–30-day filtered **a** vertical velocity (interval: 10^{-2} Pa s^{-1}), **b** vorticity (interval: 2.0×10^{-6} s^{-1}), **c** specific humidity (interval: 10^{-4} kg kg^{-1}), **d** divergence (interval: 10^{-6} s^{-1}), **e** geopotential height (interval: 2 gpm) and **f** temperature (interval: 0.1 K) associated with the westward propagating 10–30-day $\langle Q_1 \rangle$. *Shadings* exceed the 0.05 significance level. Positive (negative) value in *X*-axis means the zonal distance (°lon) to the east (west) of the convection center. *Y*-axis is pressure (hPa)

$$\frac{\partial \zeta'}{\partial t} = -\left(u\frac{\partial \zeta}{\partial x}\right)' - \left(v\frac{\partial \zeta}{\partial y}\right)' - (\beta v)' - \left(\omega\frac{\partial \zeta}{\partial p}\right)' - \left[(\zeta + f)\nabla \cdot \mathbf{V}\right]' - \left(\frac{\partial \omega}{\partial x}\frac{\partial v}{\partial p} - \frac{\partial u}{\partial p}\frac{\partial \omega}{\partial y}\right)' \quad (1)$$

where a single prime denotes the intraseasonal component; $\mathbf{V} = (u, v)$ is wind velocity vector; ∇ denotes the horizontal gradient operator. The other symbols follow convention in meteorology.

Figure 8a shows the vertical-time evolution of the vorticity anomaly tendency $(\partial\zeta/\partial t)'$ at the grid −3 longitudes (where a vorticity center appears; see Fig. 7) away from the convection center. Here the *X*-axis represents the relative time. For example, day D0 is the reference time when maximum convection occurs; D−2 (D+2) means 2-day lead (lag) from day D0. As shown, a maximum $(\partial\zeta/\partial t)'$ occurs at the mid-troposphere at day D−4. Figure 8b portrays the $(\partial\zeta/\partial t)'$ and ζ' at 500 hPa as a function of the relative time. It is seen that the maximum $(\partial\zeta/\partial t)'$ appears at day D−4, while the maximum ζ' occurs at day D0. Thus, we conduct a vorticity budget analysis at day D−4 based on Eq. (1). Figure 8c illustrates the contribution of each budget term to the vorticity tendency at day D−4. The leftmost bar is the observed $(\partial\zeta/\partial t)'$, while bars 2–7 is the six budget terms at the right hand side of Eq. (1), and the rightmost bar is the sum of the six terms. It is found that the anomalous meridional vorticity advection $(-v\partial\zeta/\partial y)'$ (bar 3) is the primary term contributes to the vorticity tendency. The advection of the planetary vorticity by the meridional wind anomaly $-\beta v'$ (bar 4) is the secondary contributing term. The similar results are also clearly seen in the vertically averaged budget analysis. However, for more specific processes, one must analyze the interaction between the different time scales in detail.

As illustrated well in Jiang et al. (2004) and WD15, the easterly vertical shear mechanism is responsible for the northward propagation taking place over the area to the south of 20°N. Taking into account the gradient of the Coriolis force which is neglected in Jiang et al. (2004), Yokoi and Satomura (2006) further revealed the northward propagation mechanisms over the BOB. For the barotropic component, the vertical shear mechanism plays a key role in the middle and upper troposphere, while the advection of the vorticity perturbation by the mean meridional flow operates in the lower troposphere. For the first baroclinic component, both the advection of the vorticity perturbation by the mean meridional flow and the planetary vorticity by the meridional wind anomaly contributes to the northward propagation. All the mechanisms mentioned above explain the northward propagation occurring from ~10°N to 20°N (see Fig. 6c, d). As mentioned in the previous subsection, we mainly emphasize that the perturbation over the STP is

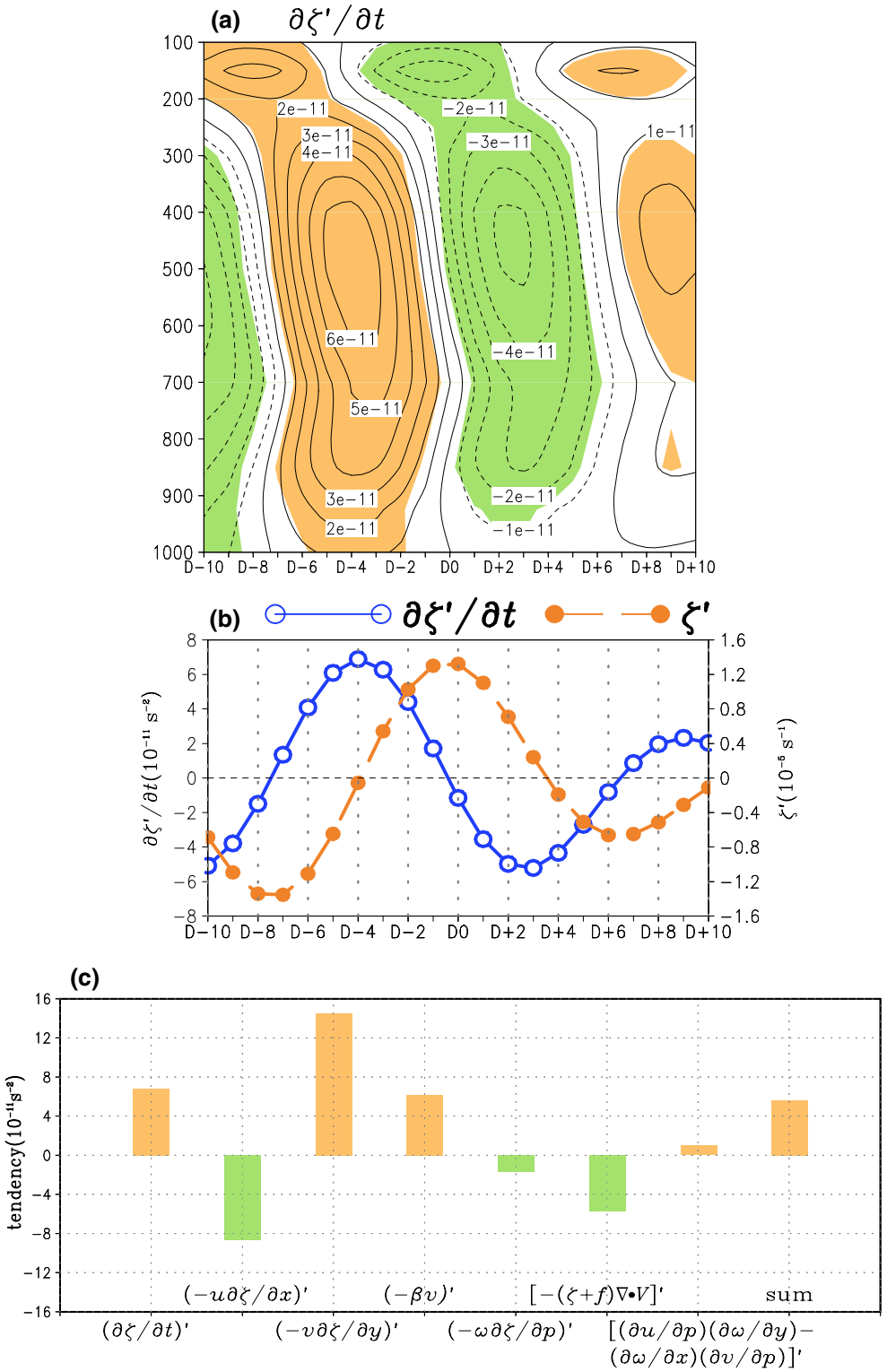

Fig. 8 **a** Time-vertical distribution of the vorticity tendency $(\partial\zeta/\partial t)'$ (unit: s^{-2}) at the grid −3°lon (see Fig. 7b). *X*-axis represents the relative time. D0 denotes the time when maximum convection occurs; D−2 (D+2) means 2-day lead (lag) from D0. *Shadings* exceed the 0.05 significance level. **b** As in (**a**), but for ζ' (*dashed line*; 10^{-5} s^{-1}) and $(\partial\zeta/\partial t)'$ (*solid line*; 10^{-11} s^{-2}) at 500 hPa. **c** The value of 500-hPa $(\partial\zeta/\partial t)'$ (*leftmost bar*), its individual terms (*bars* 2–7) and the sum of individual terms (*rightmost bar*) at the time of D−4 at −3°lon with respect to convection center

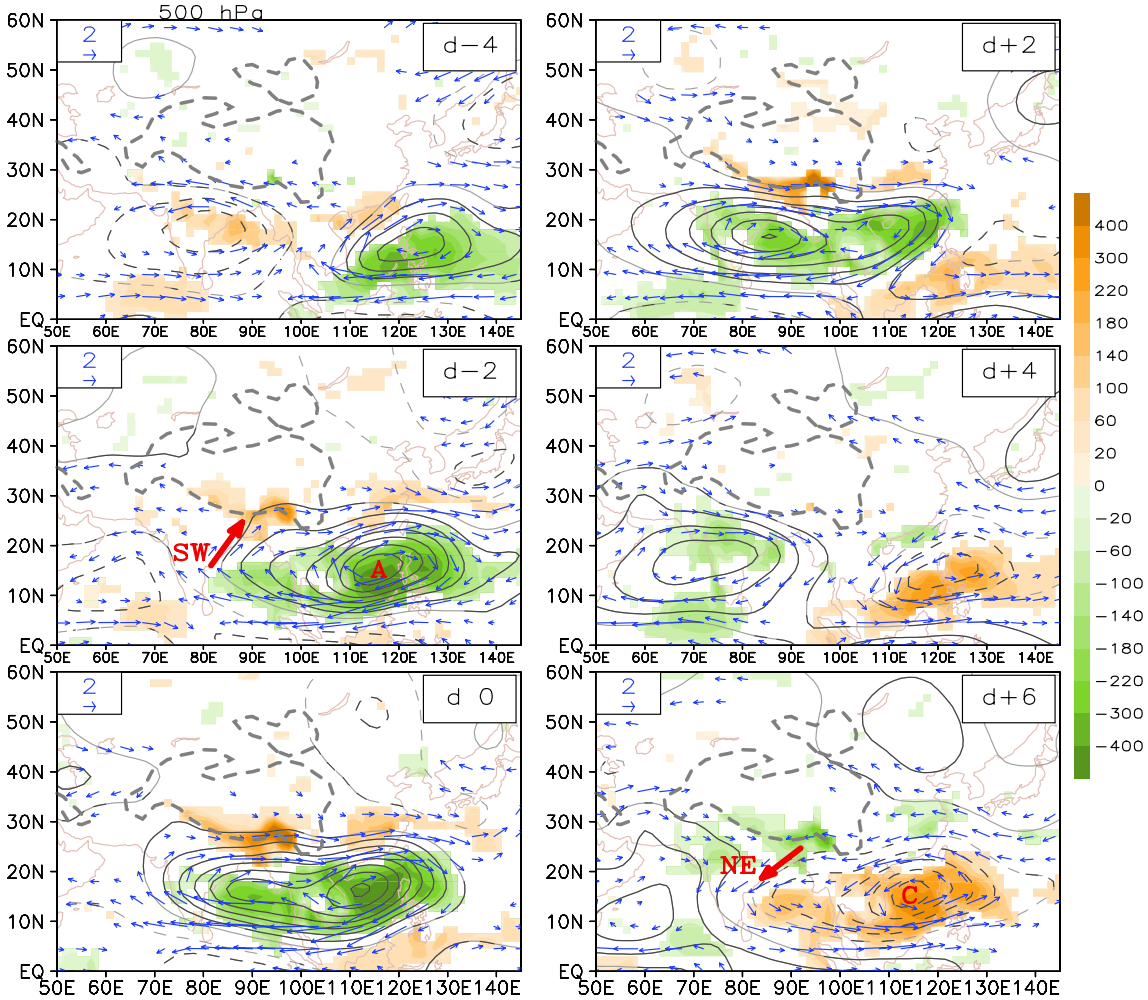

Fig. 9 Composite of 10–30-day filtered $\langle Q_1 \rangle$ (*shading*; W m^{-2}), 500-hPa stream function (contours with interval of 1.0 × 10^6 m^2 s^{-1}; zero contours omitted) and *horizontal* wind (*vector*, m s^{-1}). "*A*" ("*C*") denotes anticyclonic (cyclonic) anomaly; *shadings*, *vectors*, and *dark contours* exceed the 0.05 significance level

quasi-stationary and is not simple phase propagation from low latitudes. In the following, we will examine the cause of the intraseasonal variability over the STP through analyzing the evolutions and structures of the circulation at different tropospheric levels.

3.3.2 Cause of the intraseasonal variability over the STP

The temporal evolution of the lower-tropospheric circulation (not shown) associated with the $\langle Q_1 \rangle$ anomaly is highly consistent with that of the vertically integrated water vapor flux and moisture convergence anomalies shown in Fig. 5. The signal from mid-latitudes is not obvious in the lower troposphere.

The evolution patterns of the mid-tropospheric (500-hPa) circulation as well as the $\langle Q_1 \rangle$ anomaly from day −4 to +6 are displayed in Fig. 9. As shown, the evolution feature is quite similar to that in the lower troposphere, especially at low latitudes. The ISO perturbation over the STP is induced by the alternation circulation anomalies over the BOB. Once an anticyclonic anomaly propagates to the BOB, westerly/southwesterly anomaly blows into the STP (e.g., day −2), corresponding to a moisture convergence and positive $\langle Q_1 \rangle$ anomalies over the STP. Once a cyclonic anomaly propagates from the western Pacific to the BOB, easterly/northeasterly anomaly dominates around the STP (e.g., day +6), corresponding to a moisture divergence and negative $\langle Q_1 \rangle$ anomalies over the STP. Due to the westward/northwestward propagation of the ISO perturbations at low latitudes, the amplitude of the ISO perturbation over the STP gradually changes. The stationary feature of the ISO perturbation over the STP is essentially attributed to the topographical features over and around the STP, which has also been revealed in Fujinami et al. (2011) and FY14. The specific topography around the STP can be clearly seen in Fig. 1 of Fujinami et al. (2011) and FY14. In comparison with the

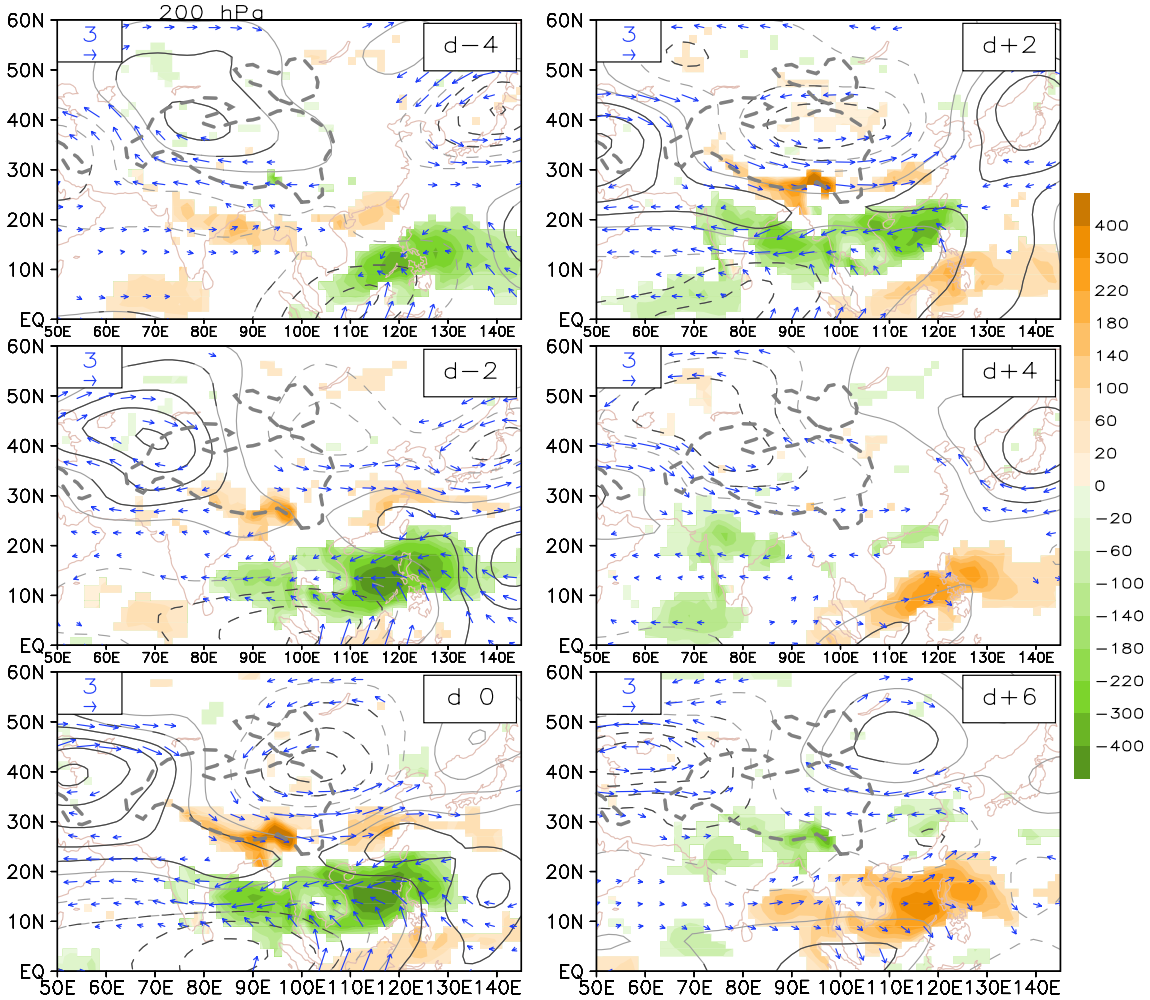

Fig. 10 As in Fig. 9, but for 200-hPa circulations

lower troposphere, the signal from mid-latitudes is a little evident in the mid-troposphere. The easterly (westerly) flow in the south flank of the anticyclonic (cyclonic) anomaly over and around Japan intrudes into the easterly (westerly) in the north/northeast flank of the cyclonic (anticyclonic) anomaly over the SCS and western Pacific, slightly strengthening the low-latitude ISO circulation.

A dominant feature of the upper-tropospheric circulation anomaly (Fig. 10) is a westward-propagating wave train along the Asian jet, which possesses a Rossby wave nature as demonstrated in FY14. Once an anticyclonic anomaly as one part of the Rossby wave train moves westward onto the TP (e.g., day −4), the STP is controlled by an easterly anomaly associated with this anticyclonic anomaly. As the Rossby waves move westward, the STP is gradually controlled by a southerly anomaly in the south flank of a cyclonic anomaly (e.g., day +2). Thus, the mid-latitudes perturbation in the upper-troposphere can enhance the zonal wind anomaly around the STP.

4 The second leading mode of diabatic heating over the TP

4.1 Spatial pattern and evolution feature

It is seen that the STD pattern of non-filtered $\langle Q_1 \rangle$ anomaly plotted in Fig. 3b exhibits an obvious difference between the eastern TP (ETP) and western TP (WTP). This indicates another leading mode of $\langle Q_1 \rangle$ anomaly over the TP. Further analysis reveals that the EOF2 pattern of the non-filtered $\langle Q_1 \rangle$ anomaly shows an asymmetric structure between the ETP and WTP (Fig. 11a). This non-filtered-based PC2 is subject to a power spectral analysis, and its statistically significant peak appears in the 10–30-day band (Fig. 11b). The EOF2 pattern of the 10–30-day filtered $\langle Q_1 \rangle$ anomaly also exhibits an east–west asymmetric structure over the TP (Fig. 11c). Note that this EOF2 pattern is statistically distinguished from higher patterns (see Table 1). In addition, the lead-lag correlation coefficients between PC1 and PC2

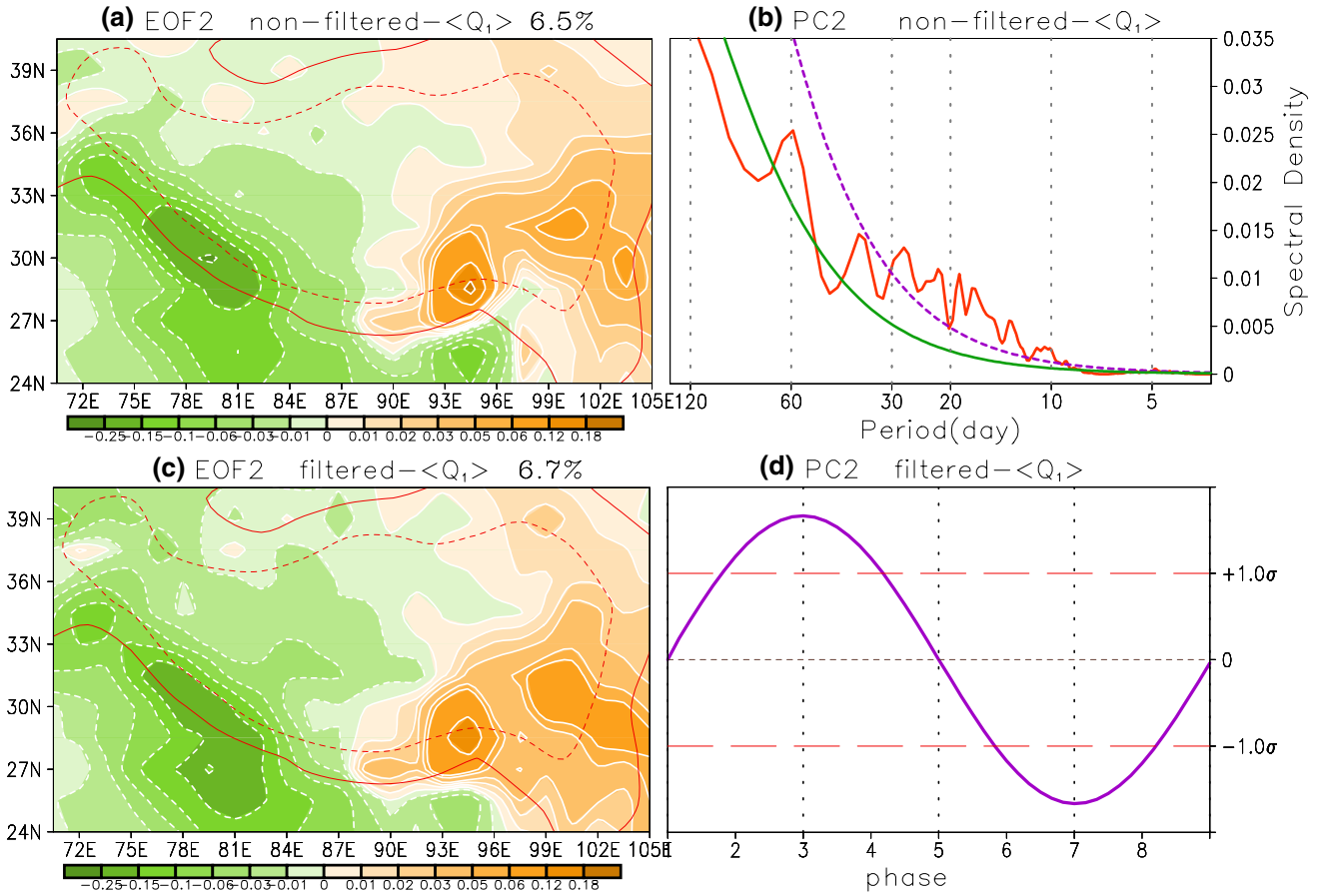

Fig. 11 EOF2 of **a** non-filtered and **c** 10–30-day filtered $\langle Q_1 \rangle$ anomaly in JJA. **b** Power spectral analysis of non-filtered-based PC2. **d** Schematic diagram of the definition of phases in terms of filtered-based PC2. *Solid* and *dashed lines* in (**b**) is spectrum density of *red* noise and the 0.01 significance level, respectively

show that there is no statistically significant correlation between them (figure omitted). It implies that the two leading modes do not represent the same physical mode over the TP.

A phase composite technique, similar to FY04, is used to examine the evolution features of the intraseasonal (10–30-day) variability associated with the second leading mode. In this method, each life cycle of the filtered-based PC2 is classified into eight phases (Fig. 11d). Phase 3 (phase 7) corresponds to the positive (negative) extreme of the PC2, phases 2 and 4 (phases 6 and 8) to the half of positive (negative) extreme, and phases 1 and 5 to the anomaly value of zero. To get robust results, a total of 79 cycles, in which both the positive and negative extremes exceed 1.0 standard deviation of the PC2, are used for phase composite.

Figure 12 displays horizontal distributions of the filtered $\langle Q_1 \rangle$ anomaly (shadings) from phase 1 to 8. The dotted grids exceed the 0.05 significance level according to a *t* test used by Jia et al. (2011) and Yang et al. (2013b), which is also used to test the statistical significance in the subsequent text. From phase 1 to 3, a positive anomaly gradually propagates southeastward from the northwestern to eastern TP. By phase 3, the anomaly pattern is characterized by an east–west asymmetric structure over the TP. By phase 4, most of the TP regions are under the control of a negative anomaly, except for the southeast border of the TP. The negative anomaly is originated from the southeast edge of the TP (see phase 1). The structures from phase 5 to 8 are nearly opposite to those from phase 1 to 4, respectively. Thus, the anomaly in the second mode shows a clockwise propagation over the TP, which is similar to the evolution of OLR anomaly in FY04 (see their Fig. 9).

4.2 Relationship to tropospheric circulations

Many previous researches (e.g., FY04; Ding and Wang 2007; Yang et al. 2010; WD15) pointed out the linkage of the ISO perturbation between the low- and mid-latitude regions. Is the evolution of the perturbation in the second leading mode related to the mid-latitude perturbation? How is this asymmetric structure formed? To address the

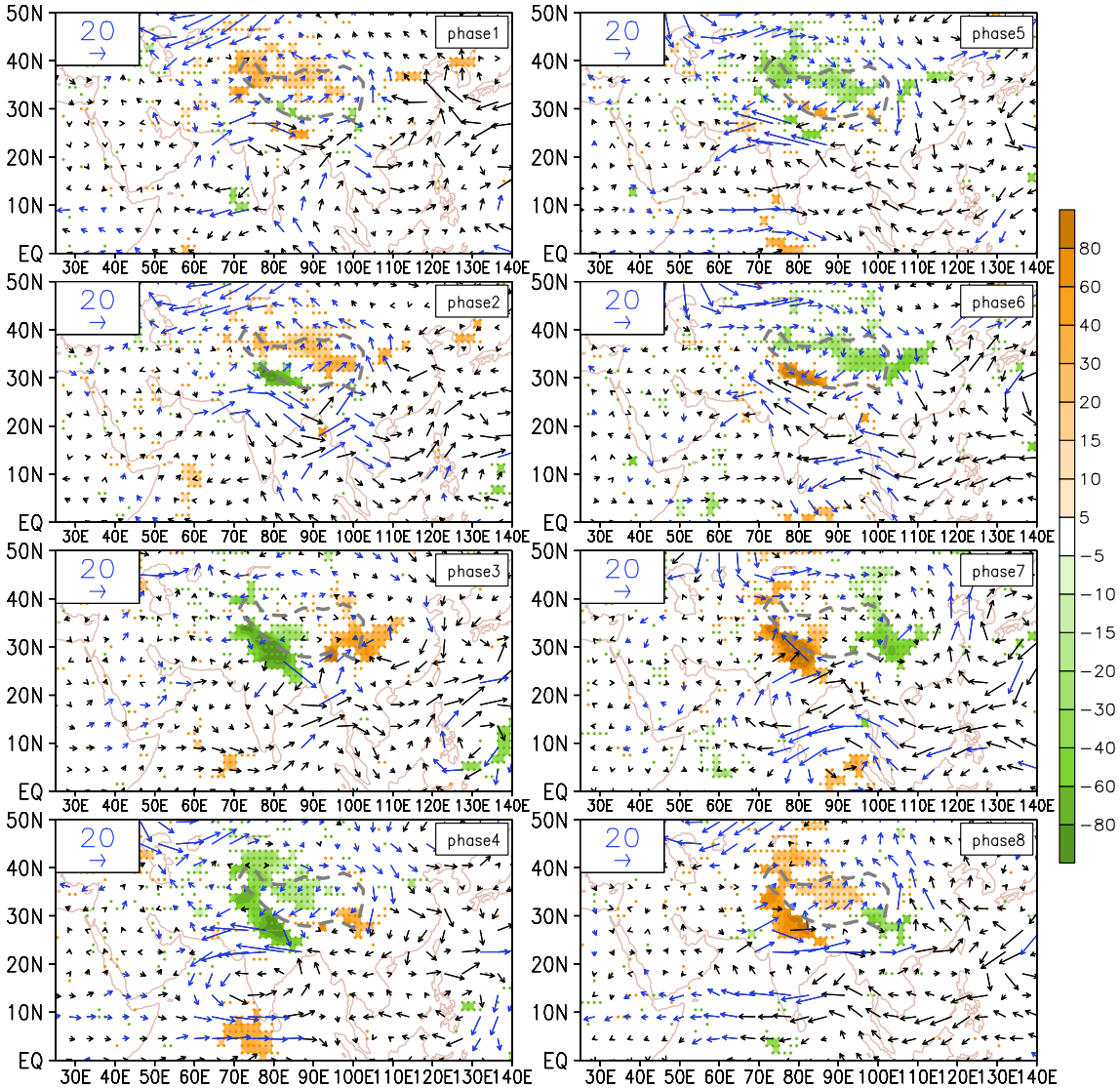

Fig. 12 Spatial distribution of composite 10–30-day filtered $\langle Q_1 \rangle$ (*shading*; W m^{-2}) and vertically integrated water vapor flux (*vector*; kg m^{-1} s^{-1}) from Phase 1 to Phase 8. *Shadings*, *dots*, and *blue vectors* exceed the 0.05 significance level. Topography exceeding 3000 m is shown by *dashed contours* (the same as below)

questions, the evolutions and structures of the large-scale circulations at different tropospheric levels are analyzed.

Figure 13 displays the evolution patterns of 200-hPa horizontal wind and stream function anomalies as well as the precipitation anomaly (41 cycles) from phase 1 to 8. Similar to FY04 (see their Fig. 10), a wave train stretches over the mid-latitude area during phase 1–8. Thus, the EOF2 mode can capture the evolution feature revealed in FY04. The wave train gradually moves southeastward/eastward from phase 1 to 8. From phase 1 to 2, an obvious anticyclonic (cyclonic) circulation as one part of the wave train governs the ETP (WTP) region. Meanwhile, the flow in the southeast/northeast flank of a 500-hPa cyclone transports water vapor onto the northern and eastern TP, inducing moisture convergence anomalies over there (shadings in Fig. 14). Thus, positive precipitation anomalies appear over the northern and eastern TP (shadings in Fig. 13), although they do not pass the 0.05 significance level over the northeastern TP. The evolution of the integrated water vapor flux (vectors in Fig. 12) suggests that the water vapor is transported from the low-latitude region. As reported in WD15, the water vapor over the central and eastern TP is also supplied from low latitudes in the active phase of the TP summer monsoon.

In phase 3, the 200-hPa anticyclone over the ETP extends eastward. It superimposes on the climatological South Asian High (FY04; Duan et al. 2008) and strengthens the east mode of the South Asian High on the intraseasonal

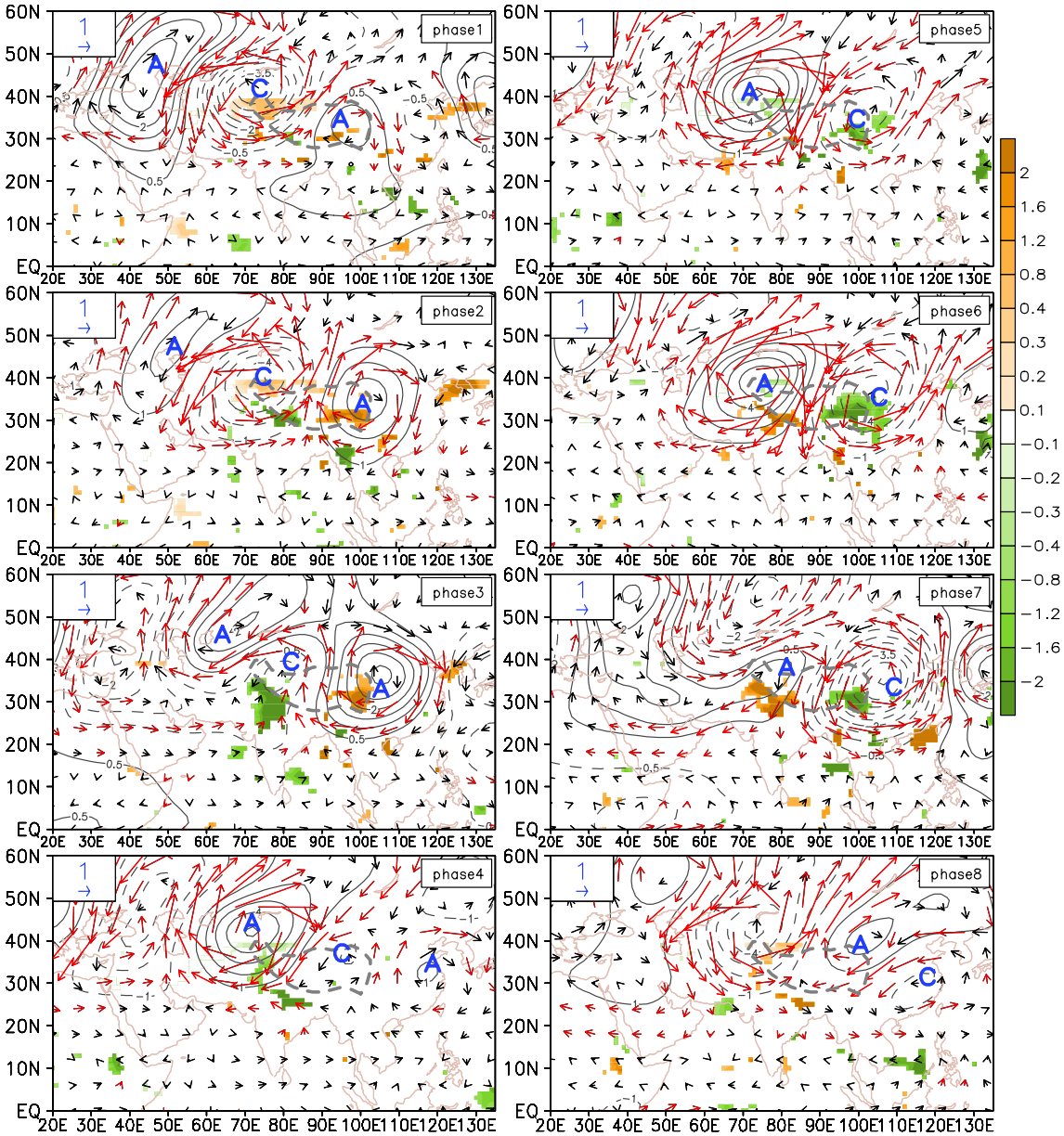

Fig. 13 As in Fig. 12, but for 10–30-day filtered GPCP precipitation (*shading*; mm day^{-1}), 200-hPa *horizontal* wind (*vector*; m s^{-1}) and stream function (contour; 10^6 m^{-2} s^{-1}); *red vectors* and *shadings* exceed the 0.05 significance level. "*C*" ("*A*") denotes cyclonic (anticyclonic) anomaly

time scale (Yang and Li 2016b), facilitating above-normal precipitation over the ETP. The water vapor over the ETP is also originated from low latitudes (see Fig. 12). At the same time, the 500-hPa cyclone moves eastward. This causes the ETP (WTP) controlled by a southerly (northerly), increasing (decreasing) the water vapor transport from the low latitudes. In phase 4, both the 200-hPa anticyclone and 500-hPa cyclone over the TP move eastward and leave the TP, and the upstream perturbations continue to move southeastward onto the TP. The signs of the anomalous fields in phase 5–8 are nearly opposite to those in phase 1–4, respectively.

The evolution patterns at 850 hPa (Fig. 15) are similar to those in the mid-troposphere. However, the transport of the water vapor from low latitudes to the TP by the ISO flow is more significant than that in the mid-troposphere.

The above analyses indicate that the upper- and lower-level waves are tightly coupled and exhibit a baroclinic structure in the troposphere over the TP. However, Kikuchi and Wang (2009) reported that in most cases, the subtropical wave trains associated with the QBWO modes show a barotropic structure. Given that most of the waves identified in Kikuchi and Wang (2009) appear over the ocean region, it is likely that the complex terrain and moist

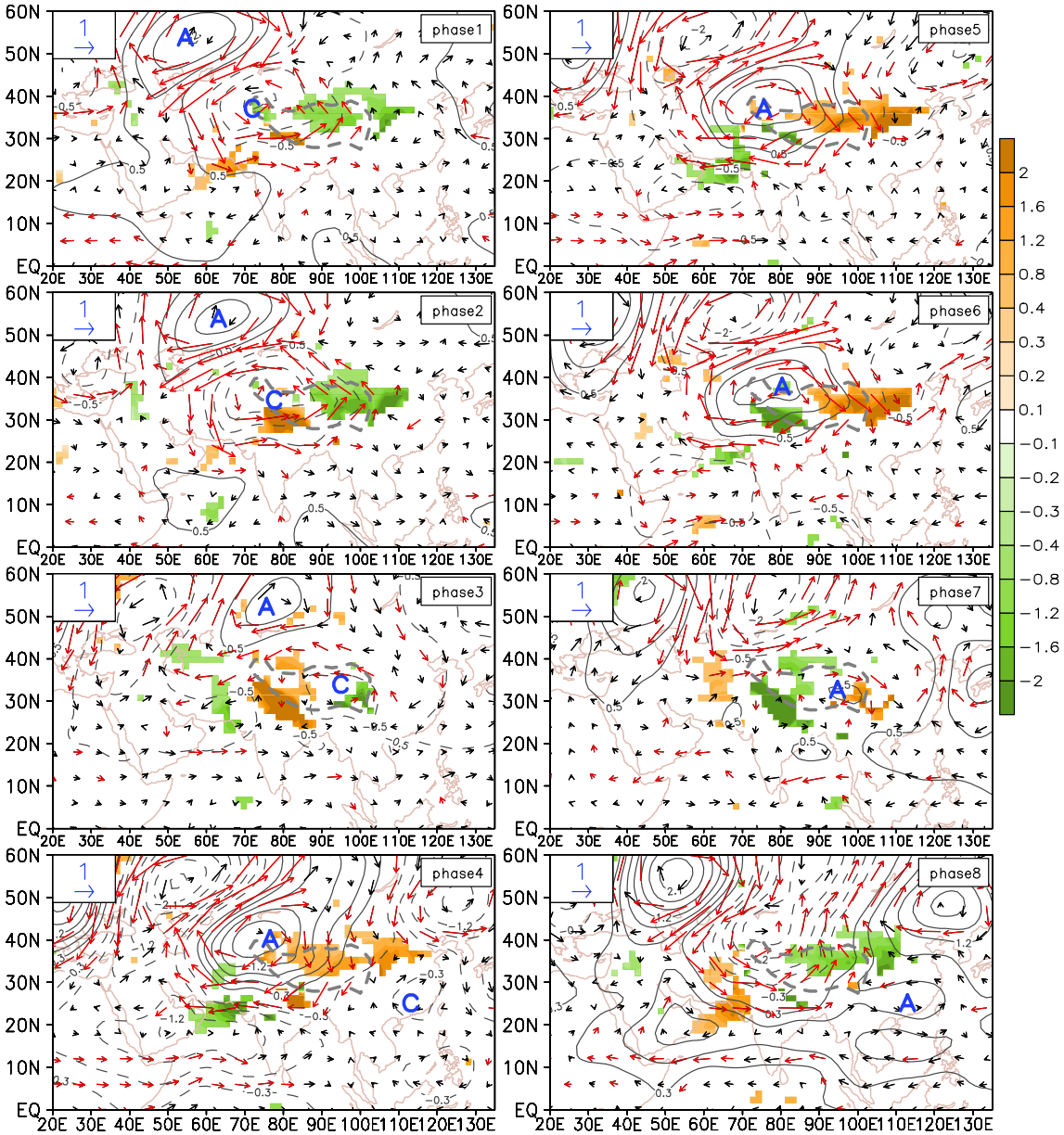

Fig. 14 As in Fig. 13, but for 10–30-day vertically integrated moisture flux divergence (*shading*; 10^{-5} kg m^{-2} s^{-1}) and 500-hPa circulations

convection over the TP play an important role in generating a baroclinic structure over the TP. The baroclinic waves associated with the QBWO mode over the TP have been reported in previous studies (e.g., FY04; WD15).

The results above suggest that the coupling of the anomalous circulation at different pressure levels plays an important role in the second leading mode. In the following, we further reveal the couplings of the vertical velocity and divergence anomaly fields. To save place, only phases 3 and 7, when the east–west asymmetric structures are established, are plotted. Figure 16a shows that at 200 hPa, a significant divergent (convergent) flow is prevalent over the ETP (WTP) in phase 3. The situation is opposite in phase 7 (Fig. 16b). The situation at 500 hPa (Fig. 16c, d) is opposite to that at 200 hPa. These upper- and lower-level configurations favor the ascending (descending) motion over the ETP (WTP) in phase 3 (Fig. 16e) and an opposite situation in phase 7 (Fig. 16f).

Different features between the ETP and WTP on the intraseasonal time scale maybe exist, similar to those on the interannual (e.g., Chen et al. 2015) and seasonal (e.g., Ueda et al. 2003) time scales. However, in order to get the different causes of the intraseasonal oscillation between the two regions, the ISO patterns over the TP should be divided

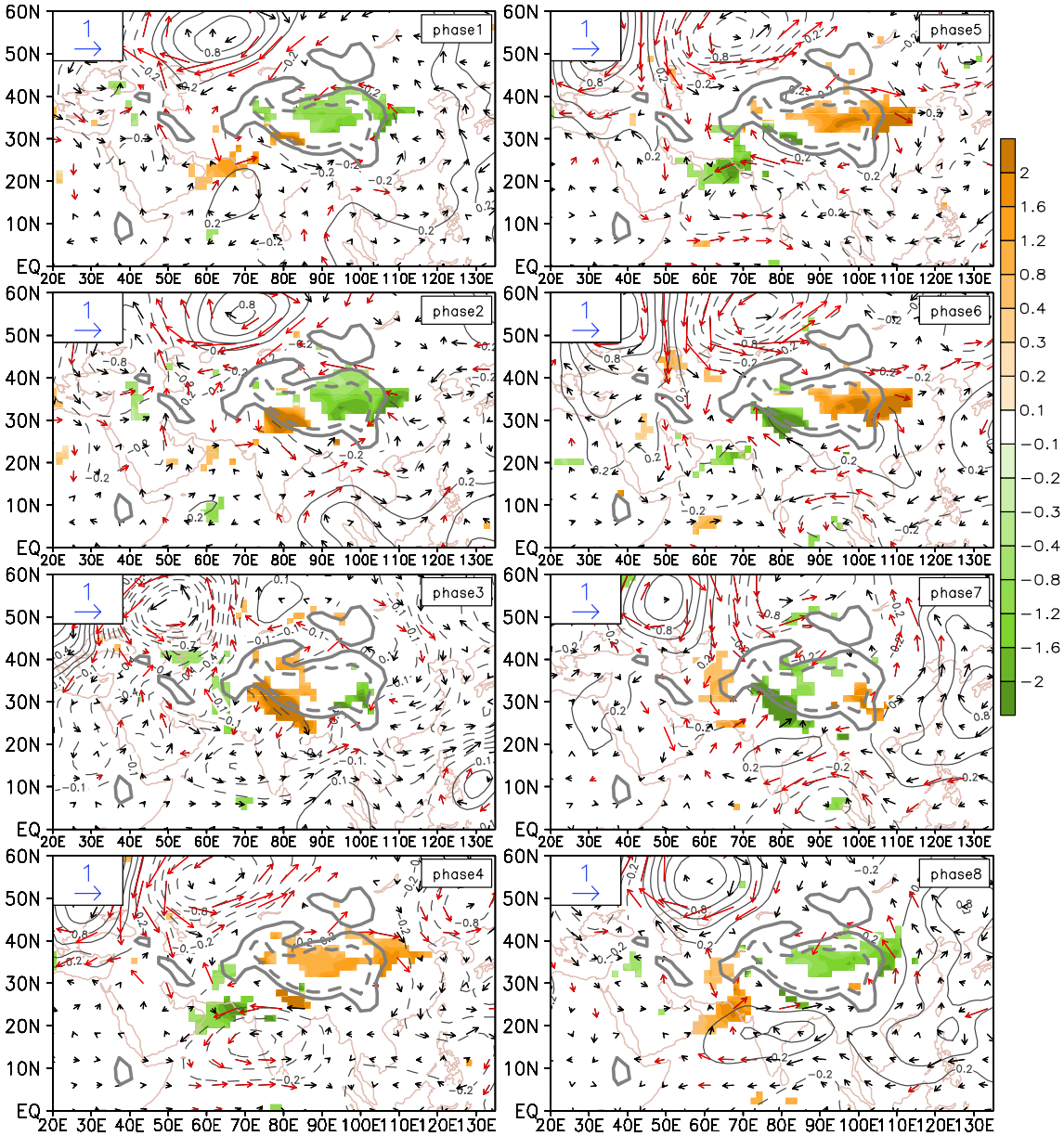

Fig. 15 As in Fig. 14, but for 850-hPa circulations; *gray solid lines* denote topography exceeding 1500 m

into an east mode and a west mode individually, which warrants further investigation in the future.

5 Summary and discussion

Two leading modes of the intraseasonal diabatic heating variability over and near the TP in boreal summer (JJA) are identified based on long-term various data. The first leading mode is characterized by a perturbation center over and near the STP. The second one is characterized by an east–west asymmetric structure over the TP. It is found that both of the modes clearly show a statistically significant 10–30-day period. Therefore, the 10–30-day anomalies associated with the two modes are analyzed.

A composite analysis reveals that the ISO perturbation over and near the STP in the first mode shows a quasi-stationary feature and is mainly related to the low-latitude ISO that is originated from the tropical western Pacific and propagates westward/northwestward from the SCS toward the northwestern India along the mean monsoon trough. The possible mechanism of the westward propagation of the ISO perturbation over the SCS is examined through a vorticity budget diagnosis, because of the striking zonal

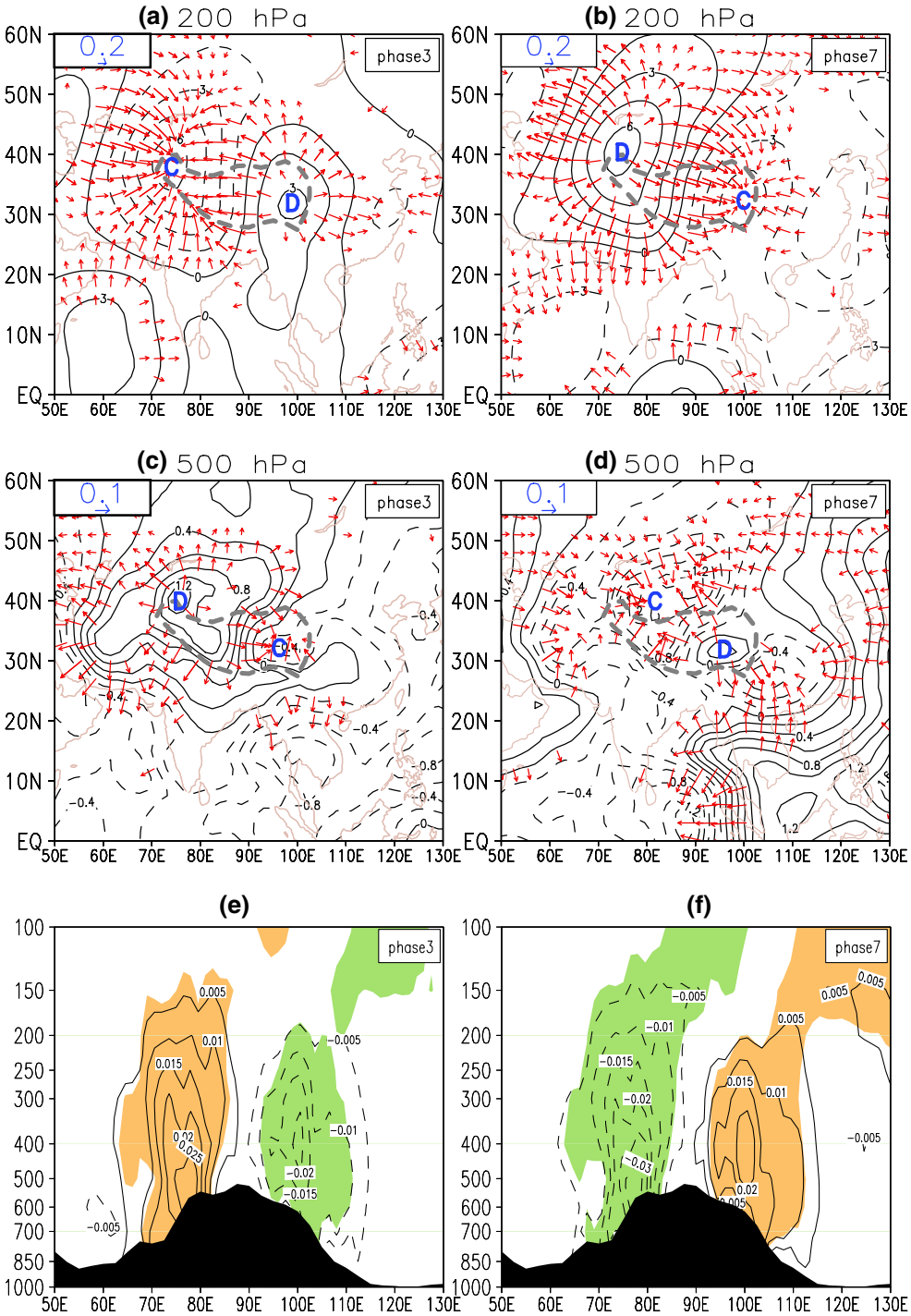

Fig. 16 10–30-day filtered **a**, **b** 200-hPa and **c**, **d** 500-hPa velocity potential (contour; 10^5 m^2 s^{-1}) and divergent wind (*vector*; m s^{-1}), and **e**, **f** zonal-vertical cross sections of vertical velocity (Pa s^{-1}) in (*left*) phase 3 and (*right*) phase 7; "*C*" ("*D*") denotes convergent (divergent) center; *vectors* and *shadings* exceed the 0.05 significance level

asymmetry of the vorticity with respect to the maximum convection. The results suggest that the dominant term that contributes to the westward propagation of the vorticity anomaly is the anomalous meridional vorticity advection, and the secondary contributing term is the advection of the planetary vorticity by the meridional ISO flow.

In this study, we mainly focus on a process that leads to the formation of the first leading mode, in which the

intraseasonal diabatic heating variability over and near the STP is not directly caused by the successive propagation of the ISO at low latitudes, but by the gradual alternation between the anticyclonic and cyclonic anomalies over the BOB originated from the western Pacific in the mid-lower troposphere. Once an ISO anticyclone (cyclone) propagates from the SCS into the BOB, a westerly/southwesterly (easterly/northeasterly) prevails around the STP, leading to an anomalous moisture convergence (divergence) due to the topographical features around the STP. During the westward-propagating journey of low-latitude perturbation, the intensity of the zonal flow around the STP gradually changes, resulting in the variation in the amplitude of the perturbation over and near the STP. Further analysis indicates that the mid-latitude perturbation in mid- and upper-troposphere plays an active role in the enhancement of the zonal wind anomaly around the STP. Especially, in the upper-troposphere, the anticyclonic/cyclonic anomaly as one part of the westward-propagating wave train at mid-latitudes increases the easterly/westerly around the STP.

A phase composite analysis reveals that the diabatic heating anomaly in the second leading mode (i.e., the east–west asymmetric structure) over the TP shows a clockwise propagation over the TP. When a positive (negative) anomaly propagates southeastward from northwestern to the eastern TP and the negative (positive) anomaly originated from the southeastern TP propagates to the western TP, the east–west asymmetric structure is formed over the TP.

The formation of the asymmetric structure is closely related to the mid-latitude wave trains, which exhibit a baroclinic structure over the TP in the troposphere. The waves propagate from northwest to southeast, and mainly show an eastward propagation when crossing the TP. The coupling between lower- and upper-level perturbations over the TP plays an essential role in setting up the east–west asymmetric structure. When the ETP (WTP) is controlled by an upper-tropospheric anticyclonic (cyclonic) anomaly, it is propitious to above-normal and under-normal convection over the ETP and WTP, respectively. Simultaneously, in the mid-troposphere, the ETP and WTP are under the control of the east and west flank of a cyclonic anomaly, respectively. Furthermore, upper-level divergence and lower-level convergence is prevalent over the ETP, leading to ascending motion and positive convective heating anomalies over the ETP, which is opposite to that over the WTP. The water vapor over the TP associated with the second mode is transported from the low-latitude area, which is most obvious in the lower troposphere. Thus, upper- and lower-level perturbations are well coupled and exhibit a baroclinic structure over the TP, causing the formation of the east–west asymmetric structure.

As indicated in FY04, FY14 and WD15, there are two dominant intraseasonal modes over and around the TP, i.e., QBWO and boreal summer intraseasonal oscillation (BSISO). More than 25-day periodicity is often used to detect BSISO mode (e.g., Kikuchi et al. 2012). Thus, 10–30-day filtered perturbation in this study may catch ISO signals in both QBWO and BSISO modes. However, compared with the results in FY04, FY14 and WD15, the 10–30-day signals capture the typical features of QBWO mode rather than BSISO mode in both the TP and South Asia. The characteristics of BSISO in the tropics has been received more attention (e.g., Wang et al. 2006), while the BSISO features over the TP warrant further study. In FY04, FY14 and WD15, they have revealed a simultaneous relationship between the low- and mid-latitudes around the TP using lag-regression or lag-composite technique, indicating that tropical—mid-latitude interaction is an inherent property of ISO perturbation on QBWO mode around the TP. Thus, although the first two leading modes seem independent from each other, they can concur over and near the TP during summer time.

Acknowledgements The authors are grateful to anonymous reviewers for their constructive comments and suggestions. This work was supported by China 973 Project 2015CB453200, NSFC Projects 416 30423/41475084/41375095/41575052, NSF AGS-1565653, NRL Grant N00173-16-1G906, Jiangsu NSF Key Project BK20150062, and Jiangsu Shuang-Chuang Team (R2014SCT001). This is SOEST contribution Number 9872, IPRC contribution Number 1226, and ESMC contribution Number 136.

References

Anderson JR, Rosen RD (1983) The latitude-height structure of 40–50 day variations in atmospheric angular momentum. J Atmos Sci 40:1584–1591

Annamalai H, Slingo JM (2001) Active/break cycles: diagnosis of the intraseasonal variability of the Asian summer monsoon. Clim Dyn 18:85–102

Bi M, Li T, Peng M, Shen X (2015) Interactions between Typhoon Megi (2010) and a low-frequency monsoon gyre. J Atmos Sci 72:2682–2702

Bretherton CS, Widmann M, Dymnikov VP, Wallace JM, Bladé I (1999) The effective number of spatial degrees of freedom of a time-varying field. J Clim 12:1990–2009

Chatterjee P, Goswami B (2004) Structure, genesis and scale selection of the tropical quasi-biweekly mode. Q J R Meteorol Soc 130:1171–1194

Chen TC, Chen JM (1993) The 10–20-day mode of the 1979 Indian monsoon: its relation with the time variation of monsoon rainfall. Mon Weather Rev 121:2465–2482

Chen J, Wu X, Yin Y, Xiao H (2015) Characteristics of heat sources and clouds over eastern China and the Tibetan Plateau in boreal summer. J Clim 28:7279–7296

Chen M, Li T, Shen X, Wu B (2016) Relative roles of dynamic and thermodynamic processes in causing evolution asymmetry between El Niño and La Niña. J Clim 29:2201–2220

Cui X, Graf HF (2009) Recent land cover changes on the Tibetan Plateau: a review. Clim Change 94:47–61

Dee D, Uppala S, Simmons A, Berrisford P, Poli P, Kobayashi S, Andrae U, Balmaseda M, Balsamo G, Bauer P (2011) The

ERA-interim reanalysis: configuration and performance of the data assimilation system. Q J R Meteorol Soc 137:553–597
Ding Q, Wang B (2007) Intraseasonal teleconnection between the Eurasian wave train and Indian monsoon. J Clim 20:3751–3767
Duan A, Wu G (2005) Role of the Tibetan Plateau thermal forcing in the summer climate patterns over subtropical Asia. Clim Dyn 24:793–807
Duan A, Wu G, Liang X (2008) Influence of the Tibetan Plateau on the summer climate patterns over Asia in the IAP/LASG SAMIL model. Adv Atmos Sci 25:518–528
Duan A, Wang M, Lei Y, Cui Y (2013) Trends in summer rainfall over China associated with the Tibetan Plateau sensible heat source during 1980–2008. J Clim 26:261–275
Duchon C (1979) Lanczos filtering in one and two dimensions. J Appl Meteorol 18:1016–1022
Flohn H (1957) Large-scale aspects of the summer monsoon in South and East Asia. J Meteor Soc Jpn 35:180–186
Fujinami H, Yasunari T (2001) The seasonal and intraseasonal variability of diurnal cloud activity over the Tibetan Plateau. J Meteor Soc Jpn 79:1207–1227
Fujinami H, Yasunari T (2004) Submonthly variability of convection and circulation over and around the Tibetan Plateau during the boreal summer. J Meteor Soc Jpn 82:1545–1564
Fujinami H, Yasunari T (2009) The effects of midlatitude waves over and around the Tibetan Plateau on submonthly variability of the East Asian summer monsoon. Mon Weather Rev 137:2286–2304
Fujinami H, Hatsuzuka D, Yasunari T, Hayashi T, Terao T, Murata F, Kiguchi M, Yamane Y, Matsumoto J, Islam M (2011) Characteristic intraseasonal oscillation of rainfall and its effect on interannual variability over Bangladesh during boreal summer. Int J Climatol 31:1192–1204
Fujinami H, Yasunari T, Morimoto A (2014) Dynamics of distinct intraseasonal oscillation in summer monsoon rainfall over the Meghalaya–Bangladesh–Western Myanmar region: covariability between the tropics and mid-latitudes. Clim Dyn 43:2147–2166
Hamada A, Arakawa O, Yatagai A (2011) An automated quality control method for daily rain-gauge data. Global Environ Res 15:183–192
Holton JR (1992) An introduction to dynamic meteorology. Academic press, Landon
Hoyos CD, Webster PJ (2007) The role of intraseasonal variability in the nature of Asian monsoon precipitation. J Clim 20:4402–4424
Huffman GJ, Adler RF, Morrissey MM, Bolvin DT, Curtis S, Joyce R, McGavock B, Susskind J (2001) Global precipitation at one-degree daily resolution from multisatellite observations. J Hydrometeorol 2:36–50
Jia X, Yang S (2013) Impact of the quasi-biweekly oscillation over the western North Pacific on East Asian subtropical monsoon during early summer. J Geophys Res Atmos 118:4421–4434
Jia X, Chen L, Ren F, Li C (2011) Impacts of the MJO on winter rainfall and circulation in China. Adv Atmos Sci 28:521–533
Jiang X, Li T, Wang B (2004) Structures and mechanisms of the northward propagating boreal summer intraseasonal oscillation. J Clim 17:1022–1039
Kikuchi K, Wang B (2009) Global perspective of the quasi-biweekly oscillation. J Clim 22:1340–1359
Kikuchi K, Wang B, Kajikawa Y (2012) Bimodal representation of the tropical intraseasonal oscillation. Clim Dyn 38:1989–2000
Krishnamurti T, Gadgil S (1985) On the structure of the 30–50 day mode over the globe during FGGE. Tellus 37A:336–360
Krishnamurti TN, Subrahmanyam D (1982) The 30–50 day mode at 850 mb during MONEX. J Atmos Sci 39:2088–2095
Lau KM, Chan PH (1986) Aspects of the 40–50 day oscillation during the northern summer as inferred from outgoing longwave radiation. Mon Weather Rev 114:1354–1367
Li T, Wang B (2005) A review on the western North Pacific monsoon: synoptic-to-interannual variabilities. Terr Atmos Ocean Sci 16:285–314
Li C, Yanai M (1996) The onset and interannual variability of the Asian summer monsoon in relation to land-sea thermal contrast. J Clim 9:358–375
Liebmann B, Smith CA (1996) Description of a complete (interpolated) outgoing longwave radiation dataset. Bull Am Meteorol Soc 77:1275–1277
Lorenz DJ, Hartmann DL (2006) The effect of the MJO on the North American Monsoon. J Clim 19:333–343
Luo H, Yanai M (1984) The large-scale circulation and heat sources over the Tibetan Plateau and surrounding areas during the early summer of 1979. Part II: heat and moisture budgets. Mon Weather Rev 112:966–989
Madden RA, Julian PR (1971) Detection of a 40–50 day oscillation in the zonal wind in the tropical Pacific. J Atmos Sci 28:702–708
Madden RA, Julian PR (1972) Description of global-scale circulation cells in the tropics with a 40–50 day period. J Atmos Sci 29:1109–1123
Maloney ED, Hartmann DL (2000) Modulation of eastern North Pacific hurricanes by the Madden–Julian Oscillation. J Clim 13:1451–1460
Mao J, Sun Z, Wu G (2010) 20–50-day oscillation of summer Yangtze rainfall in response to intraseasonal variations in the subtropical high over the western North Pacific and South China Sea. Clim Dyn 34:747–761
Murakami T, Matsumoto J (1994) Summer monsson over the Asian continent and western North Pacific. J Meteor Soc Jpn 72:719–745
Nitta T (1983) Observational study of heat sources over the eastern Tibetan Plateau during the summer monsoon. J Meteor Soc Jpn 61:590–605
North GR, Bell TL, Cahalan RF, Moeng FJ (1982) Sampling errors in the estimation of empirical orthogonal functions. Mon Weather Rev 110:699–706
Rong X, Zhang R, Li T, Su J (2011) Upscale feedback of high-frequency winds to ENSO. Q J R Meteorol Soc 137:894–907
Sato T, Kimura F (2007) How does the Tibetan Plateau affect the transition of Indian monsoon rainfall? Mon Weather Rev 135:2006–2015
Tao S, Ding Y (1981) Observational evidence of the influence of the Qinghai–Xizang (Tibet) Plateau on the occurrence of heavy rain and severe convective storms in China. Bull Am Meteorol Soc 62:23–30
Ueda H, Kamahori H, Yamazaki N (2003) Seasonal contrasting features of heat and moisture budgets between the eastern and western Tibetan Plateau during the GAME IOP. J Clim 16:2309–2324
Wang M, Duan A (2015) Quasi-biweekly oscillation over the Tibetan Plateau and its link with Asian summer monsoon. J Clim 28:4921–4940
Wang B, Webster P, Kikuchi K, Yasunari T, Qi Y (2006) Boreal summer quasi-monthly oscillation in the global tropics. Clim Dyn 27:661–675
Wang B, Bao Q, Hoskins B, Wu G, Liu Y (2008) Tibetan Plateau warming and precipitation changes in East Asia. Geophys Res Lett 35:L14702. doi:10.1029/2008GL034330
Wang L, Li T, Zhou T, Rong X (2013) Origin of the intraseasonal variability over the North Pacific in boreal summer. J Clim 26:1211–1229
Wang Z, Duan A, Wu G (2014) Time-lagged impact of spring sensible heat over the Tibetan Plateau on the summer rainfall anomaly in East China: case studies using the WRF model. Clim Dyn 42:2885–2898

Wen M, Li T, Zhang R, Qi Y (2010) Structure and origin of the quasi-biweekly oscillation over the tropical Indian Ocean in boreal spring. J Atmos Sci 67:1965–1982

Wu G, Liu Y, Zhang Q, Duan A, Wang T, Wan R, Liu X, Li W, Wang Z, Liang X (2007) The influence of mechanical and thermal forcing by the Tibetan Plateau on Asian climate. J Hydrometeorol 8:770–789

Wu G, Liu Y, He B, Bao Q, Duan A, Jin FF (2012) Thermal controls on the Asian summer monsoon. Sci Rep 2:404. doi:10.1038/srep00404

Xu Y, Li T, Peng M (2014) Roles of the synoptic-scale wave train, the intraseasonal oscillation, and high-frequency eddies in the genesis of Typhoon Manyi (2001). J Atmo Sci 71:3706–3722

Yanai M, Esbensen S, Chu JH (1973) Determination of bulk properties of tropical cloud clusters from large-scale heat and moisture budgets. J Atmos Sci 30:611–627

Yanai M, Li C, Song Z (1992) Seasonal heating of the Tibetan Plateau and its effects on the evolution of the Asian summer monsoon. J Meteor Soc Jpn 70:319–351

Yang S, Li T (2016a) Intraseasonal variability of air temperature over the mid-high latitude Eurasia in boreal winter. Clim Dyn 47:2155–2175

Yang S, Li T (2016b) Zonal shift of the South Asian High on the subseasonal time-scale and its relation to the summer rainfall anomaly in China. Q J R Meteorol Soc 142:2324–2335

Yang J, Wang B, Wang B, Bao Q (2010) Biweekly and 21–30-day variations of the subtropical summer monsoon rainfall over the lower reach of the Yangtze River basin. J Clim 23:1146–1159

Yang S, Wu B, Zhang R, Zhou S (2013a) Relationship between an abrupt drought-flood transition over mid-low reaches of the Yangtze River in 2011 and the intraseasonal oscillation over mid-high latitudes of East Asia. Acta Meteorol Sinica 27:129–143

Yang S, Wu B, Zhang R, Zhou S (2013b) The zonal propagating characteristics of low-frequency oscillation over the Eurasian mid-high latitude in boreal summer. Sci China Earth Sci 56:1566–1575

Yang K, Wu H, Qin J, Lin C, Tang W, Chen Y (2014) Recent climate changes over the Tibetan Plateau and their impacts on energy and water cycle: a review. Global Planet Change 112:79–91

Yatagai A, Kamiguchi K, Arakawa O, Hamada A, Yasutomi N, Kitoh A (2012) APHRODITE: constructing a long-term daily gridded precipitation dataset for Asia based on a dense network of rain gauges. Bull Am Meteorol Soc 93:1401–1405

Ye D (1981) Some characteristics of the summer circulation over the Qinghai–Xizang (Tibet) Plateau and its neighborhood. Bull Am Meteorol Soc 62:14–19

Ye D, Wu G (1998) The role of the heat source of the Tibetan Plateau in the general circulation. Meteor Atmos Phys 67:181–198

Yokoi S, Satomura T (2005) An observational study of intraseasonal variations over southeast Asia during the 1998 rainy season. Mon Weather Rev 133:2091–2104

Yokoi S, Satomura T (2006) Mechanisms of the northward movement of submonthly scale vortices over the Bay of Bengal during the boreal summer. Mon Weather Rev 134:2251–2265

Zhang Y, Li T, Wang B, Wu G (2002) Onset of the summer monsoon over the Indochina Peninsula: climatology and interannual variations. J Clim 15:3206–3221

Zhao P, Chen L (2001) Climatic features of atmospheric heat source/sink over the Qinghai-Xizang Plateau in 35 years and its relation to rainfall in China. Sci China Earth Sci 44:858–864

Zhou X, Zhao P, Chen J, Chen L, Li W (2009) Impacts of thermodynamic processes over the Tibetan Plateau on the Northern Hemispheric climate. Sci China Earth Sci 52:1679–1693